



## OPEN Integrated proteomics highlights functional activation induced by advanced-platelet rich fibrin plus (A-PRF +) in primary equine fibroblasts

Maria Rosaria Miranda<sup>1,2,5</sup>, Chiara Montano<sup>3,5</sup>, Valentina Golino<sup>1,4</sup>, Mariaelena de Chiara<sup>3</sup>, Chiara Del Prete<sup>3</sup>, Giacomo Pepe<sup>1,2</sup>, Davide De Biase<sup>1</sup>, Tania Ciaglia<sup>1</sup>, Alessia Bertamino<sup>1</sup>, Pietro Campiglia<sup>1</sup>, Eduardo Sommella<sup>1</sup>✉ & Maria Pia Pasolini<sup>3</sup>

Wounds are common in equine practice, and often lead to complications such as infections, delayed healing and hypertrophic scarring, which can be costly and difficult to manage. Developing affordable and effective treatments has become an increasingly important focus in veterinary research. Equine advanced-platelet-rich fibrin plus (A-PRF+) demonstrates regenerative properties comparable to its human counterpart, but cellular-level investigations exploring its molecular mechanisms remain limited. This study aimed to investigate the *in vitro* effects of equine A-PRF + on primary fibroblast cell cultures. The secretome analysis of A-PRF + revealed a complex protein profile involved in matrix remodelling, cell proliferation, and inflammation. Treatment with this platelet concentrate resulted in increased cell proliferation, enhanced migration, and significant changes in cell cycle progression compared to control groups. Reactive oxygen species production and organelles metabolism stimulation were observed, indicating active cellular responses, as well as an increase in genes and proteins associated with cell proliferation and wound regeneration. Proteomic analysis of treated fibroblasts confirmed the differential expression of key proteins associated with extracellular matrix dynamics and tissue regeneration processes. These findings provide insights into the molecular profile and functional responses of equine fibroblasts exposed to A-PRF +, contributing to our understanding of its cellular effects, supporting further exploration of this product in regenerative medicine applications.

**Keywords** A-PRF +, Tissue regeneration, Primary equine fibroblasts, Proteomics, Wound healing

In the last 50 years, the field of regenerative medicine has seen a growing interest in autologous blood-derived products, such as platelet-rich fibrin (PRF), which offer promising solutions for skin regeneration and wound healing<sup>1,2</sup>. These biomaterials leverage the natural healing potential of platelets and fibrin matrices, providing an innovative approach that minimizes the risk of immune rejection and adverse reactions<sup>3</sup>. Among these, PRF represents a second-generation platelet concentrate, produced without the use of anticoagulants or exogenous additives<sup>4</sup>. Platelets within PRF release growth factors such as platelet-derived growth factor (PDGF), transforming growth factor-beta (TGF- $\beta$ ), and vascular endothelial growth factor (VEGF), which drive cell proliferation, angiogenesis, and extracellular matrix (ECM) remodelling. Meanwhile, leukocytes contribute to immune modulation and secrete cytokines that further promote tissue repair and regeneration<sup>5–7</sup>.

Among its different formulations, advanced platelet-rich fibrin plus (A-PRF+) stands out for its enhanced bioactivity. It represents a refined PRF variant produced using an optimized centrifugation protocol that enriches its content of platelets, leukocytes, and bioactive factors while extending their release. These properties make A-PRF + particularly suited for promoting cell proliferation, migration, and tissue repair<sup>4,8–13</sup>.

<sup>1</sup>Department of Pharmacy, University of Salerno, 84084 Fisciano, SA, Italy. <sup>2</sup>NBFC—National Biodiversity Future Center, 90133 Palermo, Italy. <sup>3</sup>Department of Veterinary Medicine and Animal Production, University of Naples Federico II, Naples, Italy. <sup>4</sup>National PhD Program in "RNA Therapeutics and Gene Therapy", Napoli, Italy. <sup>5</sup>Maria Rosaria Miranda and Chiara Montano have contributed equally to this work. ✉email: vvestuto@unisa.it

In equine practice, chronic and acute wounds pose significant challenges, affecting animal welfare and performance<sup>14</sup>. Equine wounds typically heal by second intention, involving granulation tissue formation, contraction, and epithelialization. However, factors such as contamination, extensive tissue loss, and skin tension often prevent primary closure. Despite the natural healing process, complications such as chronic inflammation, delayed epithelialization, and poor contraction are common, particularly in distal limb wounds. These issues can lead to the development of exuberant granulation tissue, which slows down epithelialization and predisposes the wound to abrasions and infections, further delaying healing<sup>15</sup>. This is particularly challenging in distal limb wounds, where mechanical stress and limited blood supply worsen the healing process. PRF-based therapies address these challenges by accelerating healing, reducing infection risk, and promoting tissue regeneration, making them particularly suitable for large animal care<sup>16,17</sup>.

Despite its proven efficacy in clinical settings, the underlying mechanisms driving PRF's regenerative effects remain poorly understood, especially in equine cellular models<sup>9,10,12</sup>.

Therefore, the aim of this study was to evaluate the in vitro functional effects of equine A-PRF + on primary equine fibroblast cultures. A-PRF + was prepared from the autologous blood of the horses enrolled in the research, from which primary fibroblasts were also isolated. These cells serve as a key model for investigating the PRF-induced mechanisms of skin regeneration. Our results demonstrate that A-PRF + stimulates equine fibroblast proliferation, migration, metabolic activity, and cell cycle re-entry, effects that are accompanied by ROS (reactive oxygen species). The ROS-mediated response enhances mitochondrial, lysosomal, and endoplasmic reticulum activities, driving cellular function and promoting collagen synthesis and secretion of cytokines and growth factors critical for wound healing. To further explore the molecular underpinnings of these effects, real-time PCR experiments and a proteomic analysis were employed revealing the cell regenerative pathways. Collectively, our findings underscore the potential of A-PRF + as a powerful tool in equine wound management and contribute to a deeper understanding of its mechanism of action.

## Results

### A-PRF + secretome reveals key proteins involved in biological processes and cellular functions

To thoroughly characterize the protein content of the A-PRF + secretome, a detailed analysis was conducted to address the lack of comprehensive studies on this product in scientific literature. Detailed results of the identified proteins are reported in supporting information. The initial analysis, performed using the STRING enrichment, allowed the identification of significant protein interactions (Fig. 1). This analysis highlighted key biological processes (Fig. S1), cellular components (Fig. S2), and molecular functions (Fig. S3) associated with the secretome, emphasizing its crucial role in stimulating fibroblasts for tissue regeneration. STRING analysis revealed the enrichment of specific functional nodes, in which several key proteins were identified. Regarding the actin filament binding node, several proteins were identified, including Myosin heavy chain 3 (MYH3), Myosin XVIII A (MYO18A), Spectrin beta chain (SPTBN1), IQ motif containing GTPase activating protein 2 (IQGAP2), Espin like (ESPNL), and Actin related protein 3 (ACTR3). In the blood coagulation node, the identified proteins included Coagulation factor XIII A chain (F13A1), Fibrinogen gamma chain (FGG), and Proline rich and Gla domain 3 (PRRG3). For the cytoskeleton organization node, proteins such as Actin beta (ACTB), Eukaryotic elongation factor 2 kinase (EEF2K), Spermatosis associated 7 (SPATA7), Erythrocyte membrane protein band 4.1 like 4A (EPB41L4A), Ras homolog family member G (RHOG), and Lamin B1 (LMNB1) were detected. Finally, in the extracellular space node, proteins such as Beta-defensin 103 (A DEF103A), Apolipoprotein E (APOA4), von Willebrand factor C domain containing 2 like (VWC2L), Mammaglobin-A-like (LOC100629841), Growth differentiation factor 1 (GDF1), and TNF superfamily member 14 (TNFSF14) were identified.

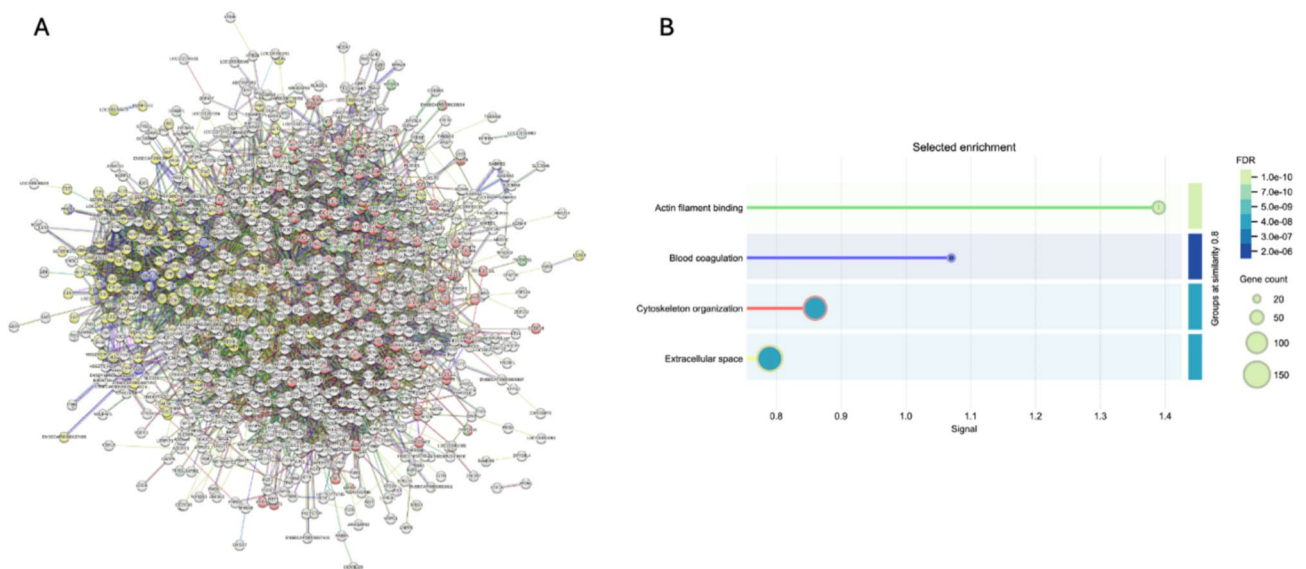


**Fig. 1.** Protein interaction analysis and functional enrichment of the A-PRF + secretome.

In image 1A, the protein–protein interaction (PPI) network generated using the STRING database is shown, highlighting the connections between the identified proteins. The colored lines represent different types of functional and physical interactions between proteins. In image 1B, the selected enrichment analysis is presented, based on the most relevant biological processes, cellular components, and molecular functions for this study. The Y-axis indicates the enriched functional categories, while the X-axis represents the statistical significance level expressed as  $-\log_{10}(\text{FDR})$ . The color of the bars reflects the FDR (False Discovery Rate) value, with lighter shades indicating higher significance. The size of the circles represents the number of genes involved in each biological process.

The resulting protein network was subjected to functional enrichment analysis using Gene Ontology (GO) and KEGG (Kyoto Encyclopedia of Genes and Genomes) (Fig. 2). KEGG analysis allowed the identification of the most represented biological pathways in the proteomic dataset, providing insights into the molecular processes involved. The proteomic analysis of the A-PRF + secretome revealed a highly specific protein composition, with predominant involvement in biological processes related to tissue repair, cytoskeleton regulation, and immune response. These findings support the potential use of A-PRF + in regenerative medicine.

### A-PRF + activates cell metabolism, stimulating proliferation and migration of primary equine fibroblasts, alongside cell cycle re-entry

To investigate the effects of A-PRF + on primary equine fibroblasts, we first assessed its impact on cellular metabolic activity. Using the MTT assay, we observed a significant increase in mitochondrial metabolism activity in A-PRF + -treated cells compared to both Ctrl (medium without FBS) (Ctrl:  $100.00 \pm 2.04\%$ , A-PRF + :  $142.20 \pm 1.15\%$ ;  $p < 0.001$  vs Ctrl) and 20% FBS (medium supplemented with 20% FBS) (A-PRF + :  $118.34 \pm 3.22\%$ ;  $p < 0.05$  vs 20% FBS), indicating an enhanced overall cellular function (Fig. 3A).

Building on this initial finding, we evaluated whether the metabolic activation correlated with increased cell proliferation. Clonogenic assays revealed a marked enhancement in colony-forming ability in A-PRF + -treated fibroblasts (Ctrl:  $100.00 \pm 4.12\%$ , A-PRF + :  $162.32 \pm 3.12\%$ ;  $p < 0.01$  vs Ctrl), with results that surpassed those observed in both control groups (20% FBS:  $137.42 \pm 5.78\%$ ;  $p < 0.05$  vs Ctrl) (Fig. 3B, C).

We then assessed the impact of A-PRF + on cell migration, a critical process for tissue repair and regeneration. Scratch wound healing assays were used to evaluate the ability of fibroblasts to close a gap created in a confluent cell monolayer. Control cells showed minimal wound closure after 24 h, as expected due to the lack of FBS, which is known to provide essential growth factors that stimulate migration. On the other hand, fibroblasts treated with 20% FBS demonstrated notable migration, leading to a substantial wound closure area after 24 h (Ctrl:  $100.00 \pm 4.54\%$ , 20% FBS:  $37.88 \pm 2.22\%$ ;  $p < 0.01$  vs Ctrl). However, A-PRF + -treated fibroblasts exhibited significantly faster and more complete wound closure within the same time frame, surpassing the effects observed with 20% FBS cells (A-PRF + :  $11.37 \pm 1.47\%$ ;  $p < 0.001$  vs Ctrl,  $p < 0.05$  vs 20% FBS) (Fig. 3D, E).

Finally, to corroborate these findings, we performed flow cytometric analyses of DNA content to assess the effects of A-PRF + on cell cycle re-entry. All cells were serum-starved for 24 h to induce quiescence. In the Ctrl

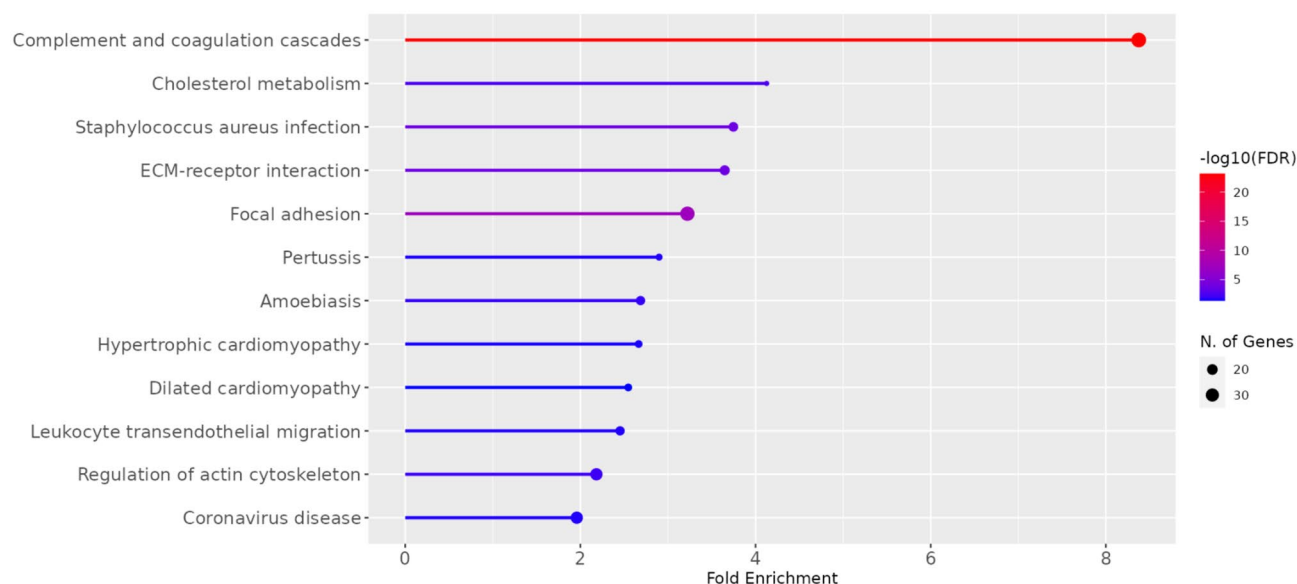


**Fig. 2.** KEGG Pathway Enrichment Analysis of the Secretome. The image presents a KEGG pathway enrichment analysis of the A-PRF + secretome, highlighting the most significantly represented biological pathways. The key elements of the analysis are: Y-axis—List of identified KEGG pathways; X-axis—Enrichment fold, indicating the extent to which a pathway is overrepresented compared to a reference set. Point color—The statistical significance of the enrichment, expressed as  $-\log_{10}(\text{FDR})$ —Intense red indicates high significance; Blue/Purple indicates lower significance; Point size—The number of genes involved in each pathway. Larger points indicate a higher number of associated proteins.

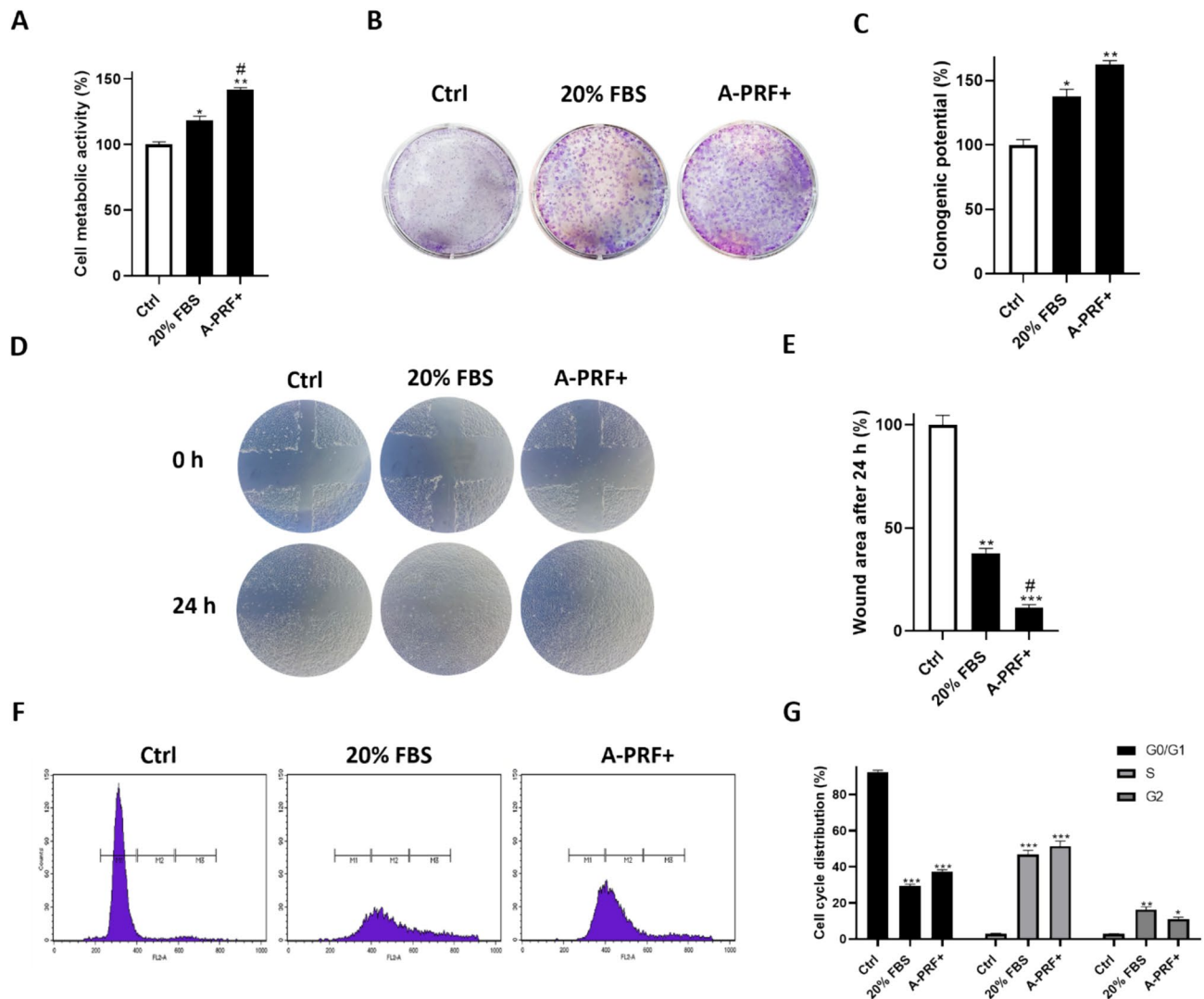


**Fig. 3.** A-PRF + improves cell function of primary equine fibroblasts. **(A)** Cell metabolism was examined by the MTT assay after 24 h of treatment. **(B)** Representative images of the clonogenic assay after 4 days. **(C)** Quantitative analysis of clonogenic potential obtained from 1% SDS cell dissolution and read to spectrophotometer. **(D)** Effect of A-PRF + on wound repair after a mechanical scratch. **(E)** Quantitative analysis expressed as wound area after 24 h. **(F)** Representative images of A-PRF + effect on cell cycle evaluated by propidium iodide assay via cytofluorimetric technique. **(G)** Quantitative analysis of DNA content. Results are expressed as mean  $\pm$  standard deviation (SD) of three independent experiments. # denotes  $p < 0.05$  versus 20% FBS; \*, \*\*, \*\*\* denote respectively  $p < 0.05$ ,  $p < 0.01$  and  $p < 0.001$  versus Ctrl.

group, where serum-free medium was maintained for an additional 24 h, a single population of quiescent cells in the G0 phase was clearly observed, as expected (G0/G1:  $92.32 \pm 1.12\%$ , S:  $3.04 \pm 0.20\%$ , G2:  $3.00 \pm 0.03\%$ ). In contrast, cells treated with 20% FBS for 24 h showed significant progression into active cell cycle phases, with a redistribution across G0/G1, S, and G2/M phases. Remarkably, A-PRF + -treated cells exhibited a similar pattern of cell cycle progression (G0/G1:  $37.39 \pm 1.04\%$ ,  $p < 0.001$  vs Ctrl; S:  $51.59 \pm 2.65\%$ ,  $p < 0.001$  vs Ctrl; G2:  $11.24 \pm 0.89\%$ ,  $p < 0.01$  vs Ctrl), with a redistribution comparable to the effects observed in the 20% FBS group (G0/G1:  $29.48 \pm 0.86\%$ ,  $p < 0.001$  vs Ctrl; S:  $48.89 \pm 2.21\%$ ,  $p < 0.001$  vs Ctrl; G2:  $16.39 \pm 1.26\%$ ,  $p < 0.05$  vs Ctrl) (Fig. 3F, G).

### A-PRF + enhances cellular function through ROS-mediated regulation of organelle activities

To further explore the mechanisms underlying the cellular improvements observed, we focused on the role of ROS production in modulating cell functions.

To evaluate the effect of A-PRF + on ROS production, we performed a time course analysis at 3, 6, and 24 h after treatment. At 24 h, ROS levels stayed high in A-PRF + and 20% FBS treatments but dropped significantly in control cells (a.u. Ctrl 24 h:  $9631.53 \pm 33.23$ , a.u. 20% FBS 24 h:  $23,928 \pm 5530.99$ ,  $p < 0.01$  vs Ctrl; a.u. A-PRF + 24 h:  $23,713.58 \pm 2296.68$ ,  $p < 0.001$  vs Ctrl), likely reflecting cellular quiescence, as shown by the previous cell cycle analysis. Furthermore, a significant increase was observed at 6 h in A-PRF + -treated cells

(a.u. A-PRF + 6 h:  $35,710.5 \pm 738.93$ , a.u. Ctrl 6 h:  $24,243.28 \pm 2095.86$ ;  $p < 0.001$  vs Ctrl) with no significant rise at 3 h. In contrast, 20% FBS treatment led to a consistent increase in ROS at both 3 and 6 h (a.u. 20% FBS 3 h:  $33,085.24 \pm 3367.24$ , a.u. Ctrl 3 h:  $22,510.54 \pm 2085.26$ ;  $p < 0.01$  vs Ctrl) (a.u. 20% FBS 6 h:  $40,789.30 \pm 1489.29$ , a.u. Ctrl 6 h:  $24,243.28 \pm 2095.86$ ;  $p < 0.001$  vs Ctrl) (Fig. 4A, B).

Following the observed increase in ROS production, we next evaluated mitochondrial activity, as mitochondria are the primary organelles associated with ROS generation. Using TMRE staining, we found a consistent increase in mitochondrial membrane potential in A-PRF + -treated cells compared to the controls, suggesting an enhancement of mitochondrial function in response to A-PRF + (a.u. Ctrl:  $15,992.12 \pm 1067.73$ , a.u. 20% FBS:  $23,138.51 \pm 652.66$ ,  $p < 0.01$  vs Ctrl; a.u. A-PRF +:  $26,039.39 \pm 1441.79$ ,  $p < 0.001$  vs Ctrl) (Fig. 4C, D).

Additionally, confocal microscopy analysis was performed to analyze mitochondrial fragmentation. Control cells exhibited elongated mitochondria, indicative of a decreased oxidative metabolism (Ctrl:  $4.24 \pm 0.03 \mu\text{m}$ )<sup>18</sup>. However, both A-PRF + and 20% FBS treatments led to increased mitochondrial fragmentation, which correlates with the ROS production observed (20% FBS:  $2.52 \pm 0.35 \mu\text{m}$ ,  $p < 0.01$  vs Ctrl; A-PRF +:  $1.65 \pm 0.62 \mu\text{m}$ ,  $p < 0.01$  vs Ctrl) (Fig. 4E, F).

To assess the impact of PRF on lysosomal activity, we measured autophagy levels using acridine orange staining. Both A-PRF + and 20% FBS-treated cells showed an increase in metabolic activity and autophagic vesicles, as confirmed by the stronger green and orange signal in treated cells compared to the untreated ones (a.u. Ctrl:  $20.16 \pm 0.87$ , a.u. 20% FBS:  $22.44 \pm 0.40$ ,  $p < 0.05$  vs Ctrl; a.u. A-PRF +:  $24.02 \pm 0.85$ ,  $p < 0.01$  vs Ctrl) (Fig. 4G, H).

Much evidence has highlighted the crucial role of endoplasmic reticulum (ER) physiological stress in cell differentiation<sup>19,20</sup>. Based on this evidence, we analyzed how ER stress affected fibroblast differentiation and proliferation through ER-specific staining. The results show that both A-PRF + and 20% FBS-treated cells increased ER-specific fluorescence intensity (a.u. Ctrl:  $12,501.75 \pm 92.94$ , a.u. 20% FBS:  $2361.25 \pm 397.65$ ,  $p < 0.01$  vs Ctrl; a.u. A-PRF +:  $3807.50 \pm 196.61$ ,  $p < 0.001$  vs Ctrl), indicating ER expansion and protein synthesis, as observed in the representative images and corresponding quantitative analysis (Fig. 4I, J).

To further validate the involvement of oxidative stress in the cellular effects induced by A-PRF +, we pre-treated primary equine fibroblasts with the antioxidant N-acetylcysteine (NAC, 2.5 mM). NAC treatment significantly reduced ROS levels in the same time course analysis at 3, 6, and 24 h after treatment (3 h: a.u. A-PRF +:  $67,304.03 \pm 1631.98$ , a.u. NAC + A-PRF +:  $49,642.18 \pm 13,555.33$ ,  $p < 0.001$  vs A-PRF +; 6 h: a.u. A-PRF +:  $85,054.55 \pm 1595.37$ , a.u. NAC + A-PRF +:  $63,457.40 \pm 7981.11$ ,  $p < 0.001$  vs A-PRF +; 24 h: a.u. A-PRF +:  $78,095.67 \pm 1268.08$ , a.u. NAC + A-PRF +:  $45,056.23 \pm 8176.93$ ,  $p < 0.001$  vs A-PRF +) (Fig. 5A) and effectively suppressed the increase in mitochondrial membrane potential ( $\Delta\Psi\text{m}$ ) (Fig. 5B, E; see first line of panel), ER expansion (Fig. 5C, E; see second line of panel), and lysosomal activity (Fig. 5D, E; see third line of panel) observed following A-PRF + administration. In addition, acridine orange staining revealed a noticeable enlargement of the cytoplasmic area in A-PRF + -treated cells, highlighted by the green signal, which was markedly reduced upon NAC treatment (Fig. 5D, E; see fourth line of panel). These findings confirm that the modulation of organelle activity by A-PRF + is at least partially mediated by ROS signaling. While this does not fully delineate the mechanistic pathway, it provides functional evidence supporting the role of oxidative stress as a key upstream regulator of A-PRF + -induced cellular responses.

### A-PRF + stimulates type I collagen, metalloproteinases, cytokines and growth factors production

Type I collagen expression was analysed by confocal microscopy in fibroblasts treated with A-PRF + to assess its effect on the synthesis of this key extracellular matrix protein to promote repair and remodelling. Results showed that A-PRF + fibroblasts demonstrated significantly higher values of type I collagen production ( $p < 0.01$  vs Ctrl) than both untreated ones and 20% FBS ( $p < 0.05$  vs Ctrl) positive control (Fig. 6A, B).

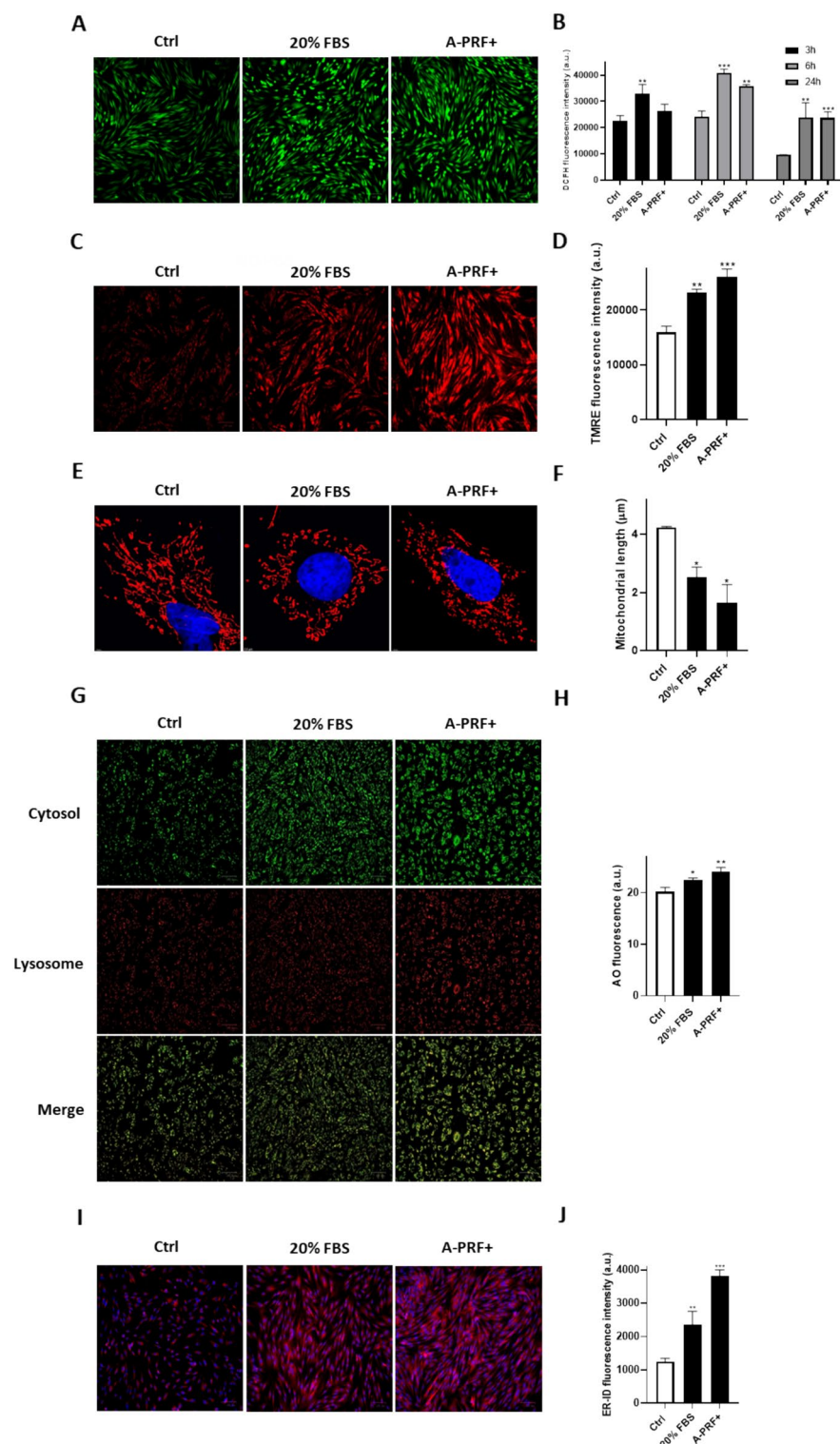
Given the well-known ability of A-PRF + to induce the expression of various growth factors in mesenchymal and endothelial cells<sup>17,21</sup>, an analysis of these growth factors was performed using real-time PCR and ELISA assays.

The increase in TGF- $\beta$ 1 expression was confirmed by real-time PCR, which demonstrated a significant difference compared to the control group ( $p < 0.001$  vs Ctrl), similarly to the treatment with 20% FBS. Likewise, A-PRF + enhanced the expression of EGF-R ( $p < 0.001$  vs Ctrl) and FGF2 ( $p < 0.01$  vs Ctrl), both involved in wound healing processes in epithelial cells and fibroblasts (Fig. 6C). These factors promote downstream signalling pathways that are necessary for the expression of MMPs in fibroblasts<sup>22,23</sup>.

Therefore, the metalloproteinases involved in extracellular matrix remodelling were analysed, and an increase in the gene expression of MT1-MMP ( $p < 0.01$  vs Ctrl), MMP2 ( $p < 0.001$  vs Ctrl), and MMP9 ( $p < 0.01$  vs Ctrl) was observed (Fig. 6D). These enzymes are key in various biological processes such as angiogenesis and wound healing<sup>24</sup>.

Increased expression of the main cytokines involved in cell proliferation and migration<sup>25–27</sup> was also validated by real-time PCR, namely IL-8 ( $p < 0.001$  vs Ctrl), IL-6 ( $p < 0.01$  vs Ctrl), and IL-10 ( $p < 0.01$  vs Ctrl) (Fig. 6E).

Finally, ELISA assays showed that fibroblasts treated with A-PRF + displayed a strong increase in the expression of PDGF-BB ( $4013.24 \pm 7.07 \text{ pg/mL}$ ,  $p < 0.001$  vs Ctrl), VEGF-A ( $107.70 \pm 2.80 \times 10^{-3} \text{ pg/mL}$ ,  $p < 0.001$  vs Ctrl), and TGF- $\beta$ 1 ( $28.46 \pm 0.04 \text{ pg/mL}$ ,  $p < 0.001$  vs Ctrl) (Fig. 6F). In particular, the release of PDGF-BB was significantly higher compared to the other growth factors over a 24 h period.



### Proteomic profile of A-PRF<sup>+</sup>-treated fibroblasts: differential regulation of key cellular processes

To gain a deeper understanding of the molecular mechanisms underlying the effects of A-PRF<sup>+</sup> treatment on fibroblasts, we performed a LFQ-proteomic analysis that revealed a detailed landscape of protein modulation in fibroblasts treated with A-PRF<sup>+</sup> or FBS 20%. As can be observed from the heatmap of the significantly modulated proteins from one-way ANOVA analysis, distinct clusters could be appreciated, emphasizing numerous differences in protein expression (up or downregulation), or stability across the treatments (Fig. 7).

In cluster 1, no modulation of protein expression was observed with the A-PRF<sup>+</sup> treatment compared to the control. The proteins in this cluster were significantly upregulated in the FBS-treated cells. The main represented pathways in cluster 1 are: Glutamate-cysteine ligase activity; Guanylate kinase activity; CD40 receptor binding; N-formyl peptide receptor activity; DNA topoisomerase type I (single strand cut, ATP-independent) activity;

◀ **Fig. 4.** A-PRF + stimulates oxidative response, mitochondrial, ER and lysosomal activities in primary equine fibroblasts. **(A)** Representative images of ROS positive cells after 24 h of treatment. Staining was performed with DCFH-DA. **(B)** Quantitative analysis of ROS production after a time course of 3, 6 and 24 h. **(C)** Representative images of TMRE positive cells after 24 h of treatment. **(D)** Quantitative analysis of TMRE positive cells after 24 h. **(E)** Representative images of mitochondrial fragmentation process after 24 h of treatment. Staining was performed with mitotracker (red, mitochondria) and Hoechst 33,342 (blue, nuclei). **(F)** Quantitative analysis of mitochondrial length. **(G)** Representative images of AO staining after 24 h of treatment. **(H)** Quantitative analysis of AO cells after 24 h. **(I)** Representative images of ER expansion after 24 h of treatment. Staining was performed with ER-ID (red, ER) and Hoechst 33,342 (blue, nuclei). **(J)** Quantitative analysis of ER expansion after 24 h. Scale bars (Figs. 4A, 4C, 4G, 4I): 100  $\mu$ m.  $N \geq 3$ . Scale bars (Fig. 4E): 2.5  $\mu$ m.  $N \geq 10$ . Results are expressed as mean  $\pm$  standard deviation (SD) of three independent experiments. # denotes  $p < 0.05$  versus FBS 20%; \*, \*\*, \*\*\* denote respectively  $p < 0.05$ ,  $p < 0.01$  and  $p < 0.001$  versus Ctrl.

Glucokinase activity; Hexokinase activity; Beta-N-acetylhexosaminidase activity; Neurotrophin TRKA receptor binding; Cytokine activity (See the full protein list for this cluster in Supporting Information, Table S1).

In cluster 2, proteins are upregulated in both the A-PRF + and FBS 20% treatments compared to the control, and contextually the enriched pathways in cluster 2 are: Transferrin receptor activity; Bis(5-adenosyl)-triphosphatase activity; Alanine-tRNA ligase activity; ATP:ADP antiporter activity; Calcium-dependent protein serine/threonine phosphatase activity; Serine-type endopeptidase inhibitor activity; Endopeptidase regulator activity; Peptidase regulator activity (See the full protein list for this cluster in Supporting Information, Table S2).

In cluster 3, proteins involved in cell adhesion, cytoskeletal organization, extracellular matrix interactions, and receptor-ligand signalling pathways were downregulated only in the FBS 20% treatment compared to the control, while in the A-PRF + treatment, these proteins remained stable or even increased. The most significant pathways in cluster 3 are: LIM domain binding; Adenylate cyclase binding; Phosphatidylserine binding; Structural constituent of cytoskeleton; Calcium-dependent protein binding; Modified amino acid binding; Actin filament binding; Actin binding; Phospholipid binding; Cytoskeletal protein binding (See the full protein list for this cluster in Supporting Information, Table S3).

In cluster 4, a strong upregulation of proteins was observed only in the A-PRF + treatment compared to the controls. Accordingly, this cluster was mostly enriched in pathways such as: Fructose-bisphosphate aldolase activity; Fructose binding; Aldehyde-lyase activity; Vinculin binding; Structural constituent of the post synapse; Nuclear receptor coactivator activity; Nuclear receptor activity; Carbon-carbon lyase activity; Protein-containing complex binding (See the full protein list for this cluster in Supporting Information, Table S4).

Finally, in cluster 5, a downregulation of proteins was observed in both the A-PRF + and 20% FBS treatments compared to the control cells, that was associated to pathways such as trans-2-enoyl-CoA reductase (NADPH) activity; Death effector domain binding; Chromatin insulator sequence binding; Caspase binding; Roundabout binding; Death receptor binding; Pattern recognition receptor activity; Oxidoreductase activity, acting on the CH-CH group of donors, NAD or NADP as acceptor; Transcription coregulator binding; Signalling receptor binding (See the full protein list for this cluster in Supporting Information, Table S5). The detailed analysis of these clusters will be presented in the discussion section, focusing on the specific proteins and their functional roles.

In this analysis, the objective was to identify distinctive expression patterns across different experimental conditions and to detect potential biomarkers or differentially expressed genes. The most relevant cluster is cluster 4, as it exhibits a markedly differential modulation of proteins in fibroblasts treated with A-PRF + compared to both positive and negative controls. This result suggests that the therapeutic effect could be predominantly concentrated within this cluster, in which different proteins have been identified. Proteins such as Solute Carrier Family 33 Member 1 (A0A9L0S635), Alpha-actinin-1 (F7D837), and Fructose-bisphosphate aldolase (A0A3Q2L254), which are involved in cellular signaling, cytoskeletal dynamics, and energy metabolism, show marked upregulation post-treatment. Solute Carrier Family 33 Member 1, involved in acetylcholine transport, may modulate neuroinflammatory responses, thereby influencing fibroblast activity. Alpha-actinin-1, a key component of the cytoskeleton, is critical for maintaining cell shape and adhesion, facilitating fibroblast migration during tissue remodelling. Additionally, Fructose-bisphosphate aldolase, part of the glycolytic pathway, supports the increased energy demands of fibroblasts as they proliferate and synthesize extracellular matrix components<sup>28,29</sup>.

Furthermore, proteins involved in ribosome biogenesis, such as Ribosome Biogenesis Protein BOP1 (F6XI32), and those associated with chromatin remodelling, like Actin-like Protein 6A (K9K2R4), are also upregulated. These proteins are vital for cell growth and transcriptional regulation, ensuring proper cellular function in the context of regeneration. The upregulation of MAGUK p55 Scaffold Protein 3 (F7DEC9) and Zinc Finger Proteins (F7CPY0, F6YET1) further supports enhanced fibroblast signalling and transcriptional activity, essential for regenerative response<sup>30,31</sup>.

The overexpression of Cilia and Flagella Associated Protein 92 (A0A9L0TUN8) suggests that cilia function may play a role in mechanosensation and cellular signalling during the regenerative process. This protein's involvement could be linked to enhanced fibroblast responsiveness to mechanical stimuli, a key aspect of tissue regeneration (Table S4).

Additionally, a gene ontology analysis was conducted to identify the ten most significant pathways in which the involved proteins play a key role (Fig. 8A). These pathways have been highlighted to provide a better understanding of the biological processes affected by the treatment.

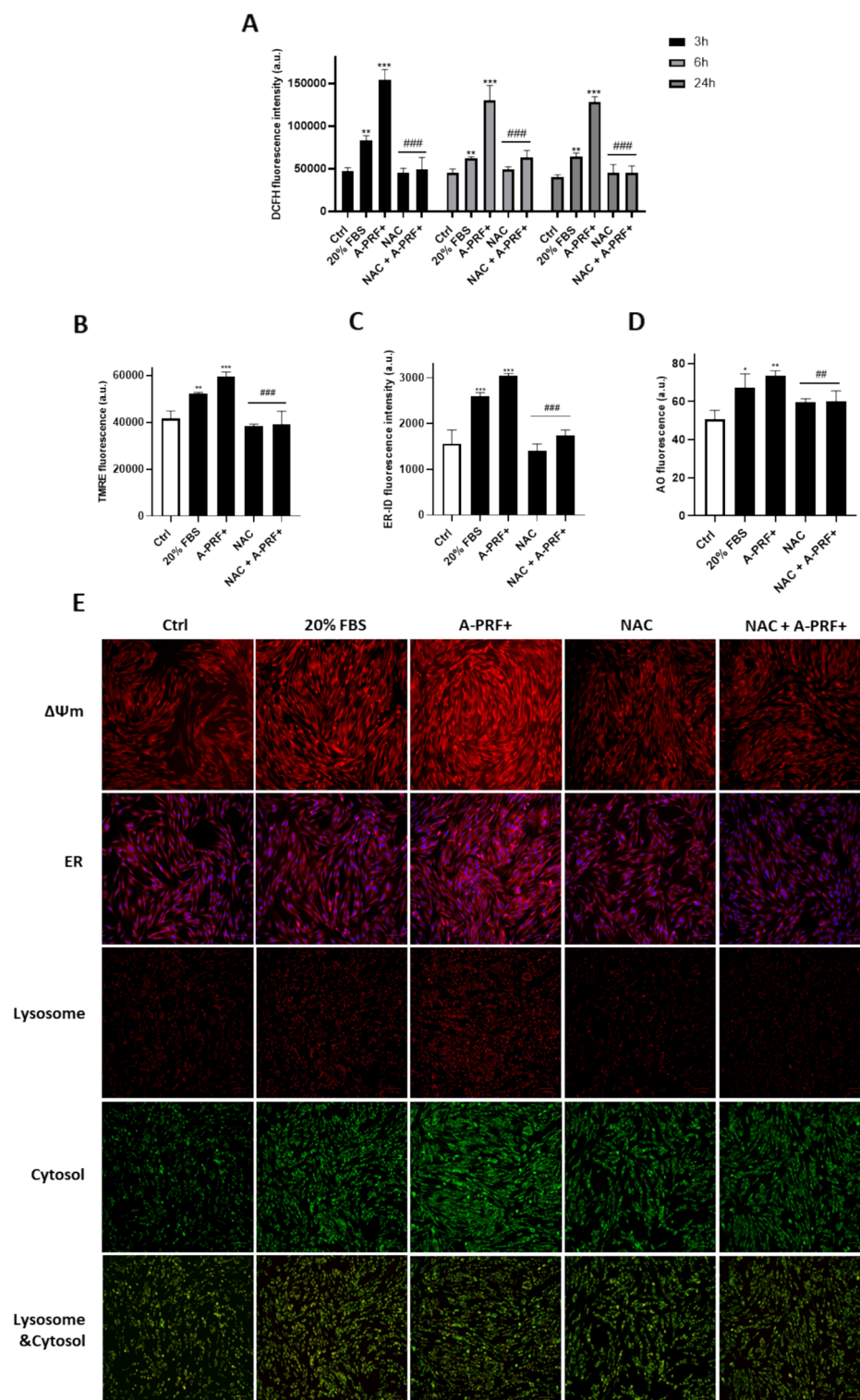


**Fig. 5.** A-PRF + stimulates mitochondrial, ER and lysosomal activities in primary equine fibroblasts through ROS signaling. (A) Quantitative analysis of ROS production after a time course of 3, 6 and 24 h. (B) Quantitative analysis of TMRE positive cells after 24 h. (C) Quantitative analysis of ER expansion after 24 h. (D) Quantitative analysis of AO cells after 24 h. (E) Representative images of mitochondrial membrane potential  $\Delta\Psi_m$  (first line), ER expansion (second line), lysosomes (third line), cytosol (fourth line), merge of cytosol and lysosome (fifth line) after 24 h of treatment. NAC (N-acetyl cysteine, 2.5 mM) was used as oxidative response inhibitor. Scale bars: 100  $\mu$ m.  $N \geq 3$ . Results are expressed as mean  $\pm$  standard deviation (SD) of three independent experiments. \*, \*\*, \*\*\* denote respectively  $p < 0.05$ ,  $p < 0.01$  and  $p < 0.001$  versus Ctrl. ##, ### denote  $p < 0.01$  and  $p < 0.001$  versus A-PRF +.

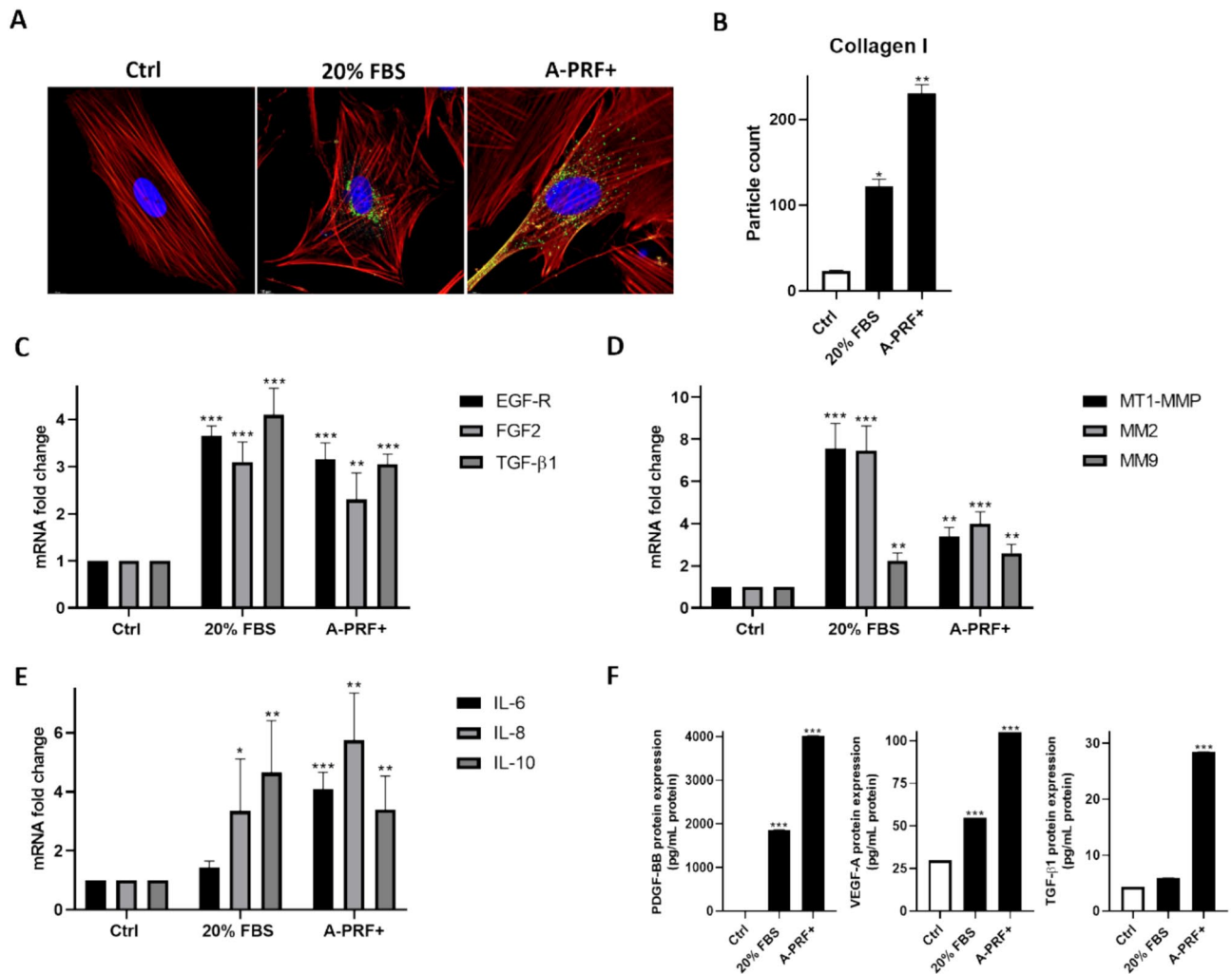


**Fig. 6.** A-PRF + increases collagen I production, cytokines, metalloproteases, growth factors gene expression and their release. (A) Confocal microscopy studies reveal collagen I production (green) after 24 h of treatment with A-PRF +. Cells are counterstained with phalloidin-tetra-methyl-rhodamine B isothiocyanate (red) and Hoechst 33,342 (blue) was used for nuclei. (B) Quantitative analysis of collagen I production. (C) Real-time PCR of EGF-R, FGF2 and TGF-β1 regenerative growth factors. (D) Real-time PCR of MT1-MMP, MMP2 and MMP9 metalloproteases. (E) Real-time PCR of IL-6, IL-8, IL-10 cytokines. (F) ELISA of PDGF-BB, VEGF-A and TGF-β1 regenerative growth factors. Scale bars (Fig. 6A: Ctrl, 20% FBS): 10 μm; Scale bar (Fig. 6A: A-PRF +): 5 μm. N ≥ 10. Results are expressed as mean ± standard deviation (SD) of three independent experiments. \*, \*\*, \*\*\* denote respectively  $p < 0.05$ ,  $p < 0.01$  and  $p < 0.001$  versus Ctrl.

In cluster 2, fibroblasts treated with A-PRF + exhibit upregulation compared to the negative control but do not show significant differences from the positive control. This suggests that the modulation of these proteins by A-PRF + occurs at a similar level to that observed in the positive control (20% FBS), indicating a comparable regulatory effect. These findings indicate that both 20% FBS and PRF treatment induces a coordinated increase in cellular activities that support fibroblast proliferation, energy production, and extracellular matrix remodelling, facilitating tissue repair and regeneration. Figure 8B reports the gene ontology analysis identifying the 10 most significant pathways in which the proteins of the cluster are involved.

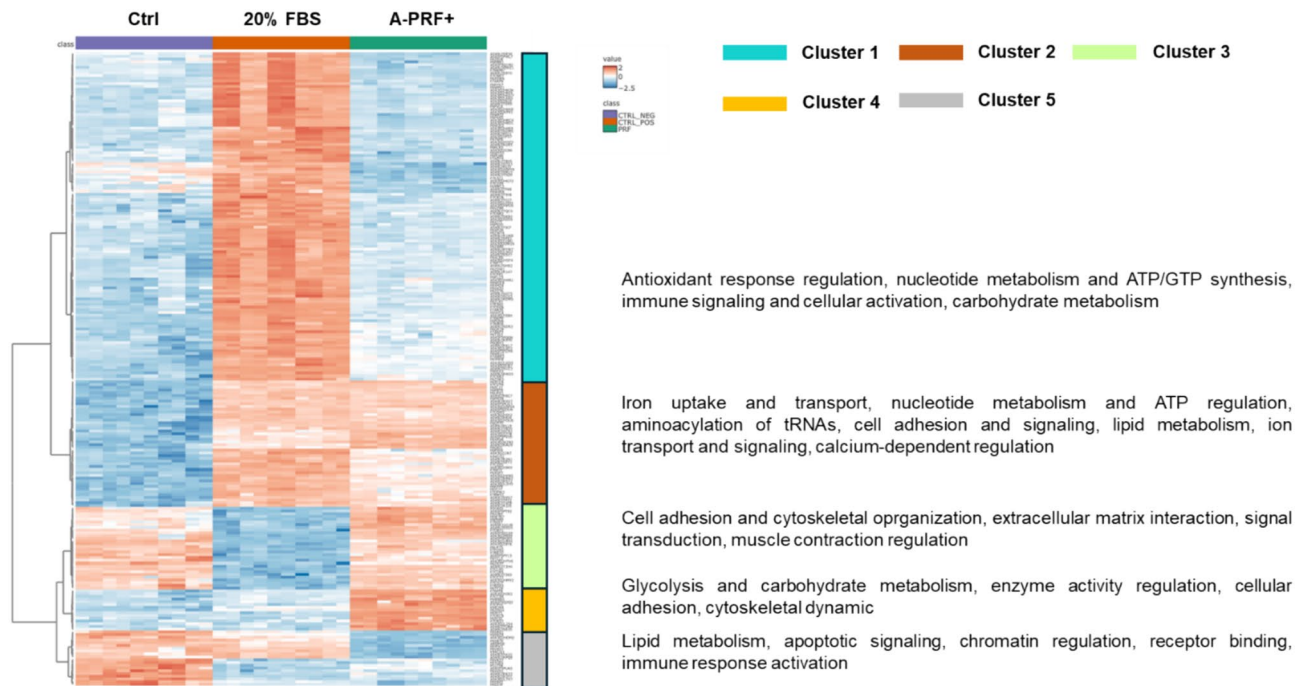
In cluster 5, the proteins present in treated fibroblasts exhibit downregulation of key proteins involved in pathways related to cell stress response, chromatin regulation, and apoptosis modulation.

Figure 8C reports gene ontology analysis identifying the 10 most significant pathways in which the proteins of the cluster are involved.

## Discussion

The study highlights the multifaceted regenerative effects of equine A-PRF +, particularly its ability to influence fibroblast behaviour and modulate key cellular processes.

First, a secretome analysis was conducted to investigate the array of bioactive factors released by cells in response to A-PRF +, providing insights into its paracrine effects and its role in orchestrating regenerative



**Fig. 7.** Heatmap of the differentially expressed proteins and pathway enrichment analysis of each protein cluster. The heatmap represents protein expression levels in a set of biological samples, with proteins displayed in rows and samples (under different experimental conditions) in columns. The colour intensity indicates normalized expression levels, with red shades representing overexpression and blue shades indicating underexpression. The analysis identified five distinct clusters with differentiated expression profiles. Each cluster has been highlighted, and next to the heatmap, the main biological pathways in which the involved proteins actively participate have been reported.

processes. Among the biological processes, the secretome was strongly linked to supramolecular fiber organization, cytoskeleton reorganization, and plasma membrane-bounded cell projection organization<sup>32–35</sup>. These findings suggest that the secretome influences collagen fiber assembly and stabilization, processes essential for extracellular matrix (ECM) formation and fibroblast adhesion. The modulation of cytoskeletal dynamics highlights its role in actin filament and microtubule remodelling, which are crucial for fibroblast migration and contractile activity during tissue repair. The involvement in the organization of plasma membrane projections, such as lamellipodia and filopodia, further supports its ability to enhance cellular motility and interaction with the ECM during regeneration<sup>9,10,36,37</sup>.

At the cellular component level, the secretome was enriched in structures such as the histone deacetylase complex, brush border, basement membrane, actin filaments, microtubules, collagen-containing ECM, and cortical cytoskeleton. These associations underscore its role in stabilizing the extracellular environment, supporting fibroblast adhesion, and maintaining the structural integrity necessary for effective tissue remodelling. Furthermore, the enrichment of histone deacetylase complexes points to a regulatory influence on fibroblast gene expression, allowing them to adapt dynamically to the regenerative cues provided by the secretome.

At the molecular level, the secretome exhibited scaffold protein binding, microtubule motor activity, cytoskeletal motor activity, actin filament binding, histone binding, GTPase regulatory activity, protein serine/threonine kinase activity, and ATP-dependent helicase activity. These functions highlight its capacity to regulate intracellular transport, cytoskeletal remodelling, and signal transduction pathways. For instance, scaffold protein binding facilitates the assembly of signalling complexes that drive fibroblast-mediated ECM remodelling and migration, while motor activities and filament-binding proteins support cytoskeletal dynamics and intracellular transport, both of which are critical for efficient tissue repair. GTPase regulatory activity suggests that the secretome actively influences the dynamics of cytoskeletal elements such as actin filaments and microtubules<sup>38–42</sup>. Small GTPases, including members of the Rho, Rac, and Cdc42 families, are known to regulate cytoskeletal remodelling by orchestrating processes like actin polymerization, microtubule stability, and intracellular transport. The presence of tubulin-binding proteins further supports this connection, highlighting the secretome role in modulating microtubule assembly and disassembly, critical for fibroblast migration and mechanotransduction. Additionally, the presence of histone-binding proteins and kinases suggests that the secretome influences epigenetic and post-transcriptional regulation, further enhancing fibroblast functionality<sup>43–47</sup>. Collectively, these findings reveal the A-PRF + secretome as a biologically active and multifunctional product that orchestrates a wide range of processes crucial for tissue regeneration. Its ability to modulate ECM assembly, cytoskeletal reorganization, and intracellular signalling positions it as a potent tool for enhancing fibroblast activity in regenerative medicine applications.

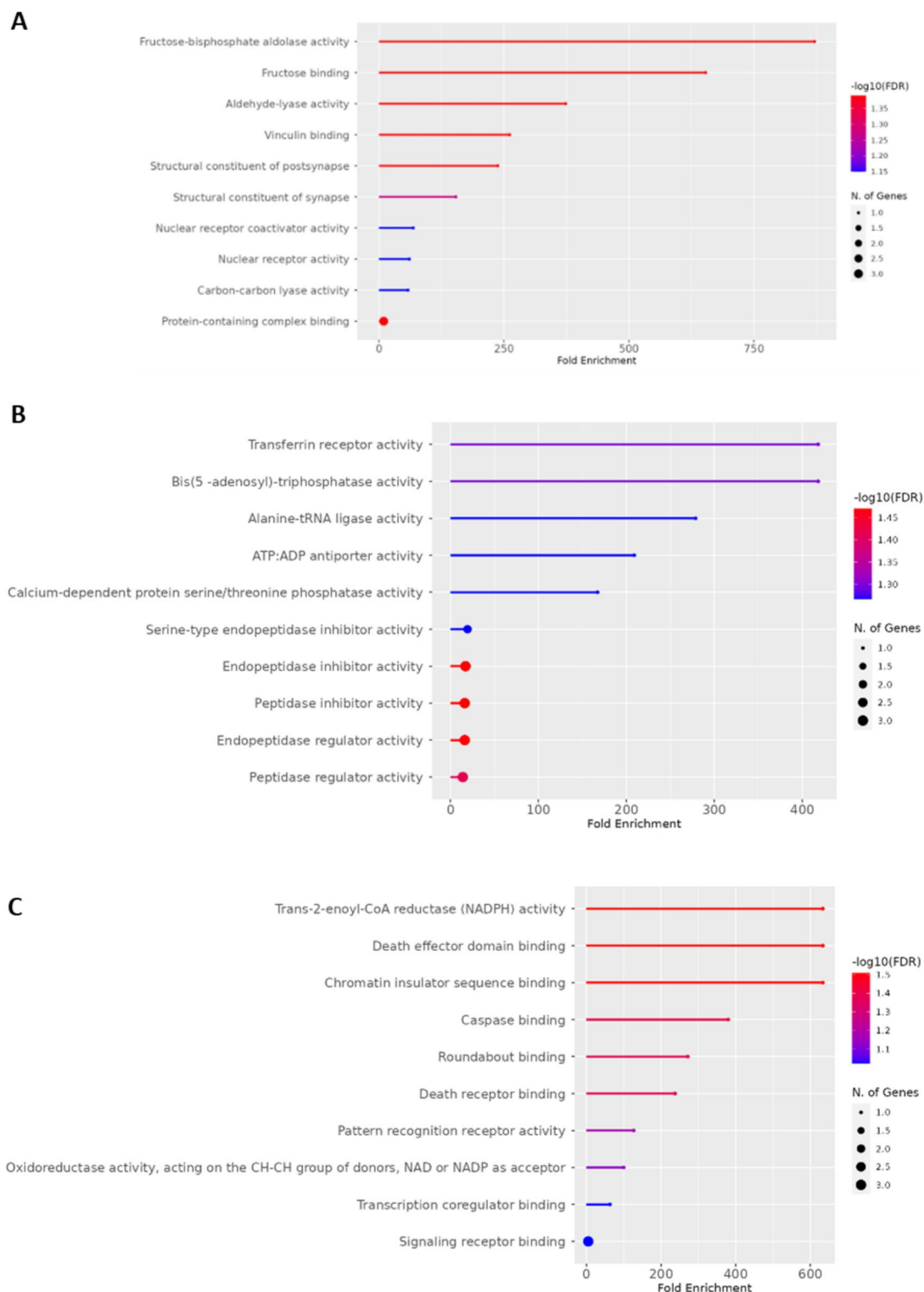


**Fig. 8.** (A) Molecular functions identified through Gene Ontology (GO) enrichment analysis of cluster 4. The top 10 pathways are displayed, with fold enrichment represented on the x-axis. Dot color indicates significance level ( $-\log_{10}(\text{FDR})$ ), while dot size reflects the number of genes associated with each pathway. (B) Molecular functions identified through Gene Ontology (GO) enrichment analysis of cluster 2. The top 10 pathways are displayed, with fold enrichment represented on the x-axis. Dot color indicates significance level ( $-\log_{10}(\text{FDR})$ ), while dot size reflects the number of genes associated with each pathway. (C) Molecular functions identified through Gene Ontology (GO) enrichment analysis of cluster 5. The top 10 pathways are displayed, with fold enrichment represented on the x-axis. Dot colour indicates significance level ( $-\log_{10}(\text{FDR})$ ), while dot size reflects the number of genes associated with each pathway.

Following the characterization of the secretome, cellular assays were performed to validate its functional effects, focusing on key processes such as fibroblast proliferation, migration, and metabolic activity. Throughout the study, 20% FBS was used as a positive control due to its well-established capacity to support cellular functions such as proliferation, migration, and metabolic activity, as well as to provide a benchmark for proteomic analysis.

FBS is one of the most enriching media used in biological research<sup>48</sup>. It serves as a source of growth factors, carbohydrates, lipids, amino acids, proteins, vitamins, and albumin, supporting cellular metabolism and cell growth. In some studies, platelet-rich plasma (PRP) has shown properties similar to FBS in stimulating cell growth<sup>49,50</sup>. However, when comparing PRP and PRF, the latter demonstrates superior regenerative capacity<sup>51,52</sup>. Consequently, the results where PRF performs equally or better than FBS seem plausible.

A-PRF+ demonstrated a positive impact across multiple cellular assays, including enhanced metabolic activity as shown by MTT assay, increased fibroblast migration and improved clonogenic potential, highlighting its stimulatory effect on cell proliferation and the regenerative potential. Furthermore, our results highlight the superior ability of A-PRF+ compared to 20% FBS to promote proliferation and cellular motility. In addition, A-PRF+ effectively stimulates cell cycle re-entry, paralleling the activation observed with 20% FBS, corroborating that the improved metabolism, proliferation, and migration observed in A-PRF+-treated fibroblasts could be associated with cell cycle reactivation.

These effects were associated with an increase in oxidative stress, a phenomenon often linked to heightened cellular activity but which, if uncontrolled, can lead to cellular damage. However, the observed increase in mitochondrial membrane permeability and fragmentation, autophagic activity, and endoplasmic reticulum expansion suggests a coordinated adaptive response, supporting regenerative processes rather than indicating pathological stress, as also confirmed by the results observed with the 20% FBS positive control. However, the patterns of ROS increase differ, suggesting that although A-PRF+ and 20% FBS similarly enhance equine fibroblast proliferation and migration, they activate distinct pathways.

These findings corroborate also with the previous MTT assay, as indicates improved mitochondrial activity, reinforcing the conclusion that A-PRF+ positively influences mitochondrial function. Furthermore, the increased fragmentation is a physiological, adaptive response to ROS generation, allowing cells to better manage the increased bioenergetic demands<sup>53–55</sup>. These results suggest improved cellular health and metabolic activity under these treatment conditions.

The pivotal role of ROS in mediating these effects was further confirmed by the use of the antioxidant NAC, which significantly attenuated the activation of mitochondria, ER, and lysosomes, underscoring the functional importance of oxidative signaling in the cellular response to A-PRF+.

These processes are closely linked to the regulation of growth factors and cytokines involved in fibroblast responses during tissue repair. Consistent with this, real-time PCR analysis revealed a modulation in the expression of key cytokines, including IL-10, IL-6, and IL-8, as well as MMPs, suggesting an active role of A-PRF+ in regulating inflammation and extracellular matrix remodelling. Additionally, the increased expression of EGFR, FGF2, and TGF- $\beta$ 1 indicates an enhancement of mitogenic and pro-regenerative signalling. These findings are further supported by ELISA results, which show an increase in the secretion of PDGF and TGF- $\beta$ 1, both crucial for fibroblast proliferation and differentiation<sup>56,57</sup>. Moreover, confocal microscopy analysis revealed an increase in type I collagen, a key component of the extracellular matrix essential for tissue strength and integrity<sup>16,58</sup>. Given its fundamental role in wound healing and remodelling, the enhanced production of type I collagen further supports the pro-regenerative effects of A-PRF+<sup>40</sup>. Overall, these results suggest that PRF exerts a coordinated effect on fibroblast dynamics by influencing both intracellular activation signals and the production of key mediators involved in tissue regeneration.

At this point, a proteomics analysis was performed to deepen the mechanistic effects of A-PRF+. This comprehensive approach allowed us to obtain a detailed protein profile from treated fibroblasts, providing valuable insights into the changes induced by A-PRF+ treatment.

Notably, proteomic studies on equine cells treated with A-PRF+ are still limited in the literature, making this analysis an important contribution to our understanding of the functional activity of secretome and the consequent cellular response to A-PRF+ and distinguish them from those influenced by 20% FBS.

In cluster 1, no modulation of protein expression was observed with the A-PRF+ treatment compared to the control. However, the proteins in this cluster were significantly upregulated in the 20% FBS-treated cells. Proteins involved in processes such as glutamate-cysteine ligase activity, guanylate kinase activity, and mannokinase activity are more sensitive to the presence of serum, which activates various signaling pathways for cell survival and proliferation. Since PRF is focused more on healing and tissue repair, rather than cell proliferation, it likely does not induce the same level of protein expression seen in FBS-treated cells. Moreover, proteins like CD40 receptor binding and N-formyl peptide receptor activity, which are associated with immune signalling, are upregulated in FBS 20%<sup>58,59</sup>. In this regard, the species mismatch between fetal bovine serum and equine fibroblasts could lead to non-specific activation of immune-related signalling pathways. This could result in increased CD40 signalling, which might promote inflammatory responses or extracellular matrix remodelling. Since A-PRF+ derives from equine blood, it is more species-homologous, meaning it is less likely to trigger such immune-like activation, explaining the absence of modulation of these immunity proteins with A-PRF+ treatment.

In cluster 2, proteins are upregulated in both the A-PRF+ and FBS 20% treatments compared to the control. This suggests that the PRF, like FBS, promotes the activation of signalling pathways involved in key cellular functions such as transferrin receptor activity, calcium-dependent protein phosphatase activity, and adenylate cyclase binding<sup>60,61</sup>. Notably, the Transferrin receptor activity pathway, which is critical for iron homeostasis and cellular respiration, is significantly upregulated, with the Transferrin receptor protein 1 (A0A3Q2GWV4) playing a central role in iron uptake. This supports enhanced metabolic activity in fibroblasts during tissue regeneration<sup>62</sup>. Additionally, proteins involved in bis(5'-adenosyl)-triphosphatase activity (e.g., bis(5'-adenosyl)-

triphosphatase (F6RYF9) are overexpressed, suggesting an increase in purine metabolism, which is essential for energy production and the regeneration process. Furthermore, the upregulation of long-chain-fatty-acid-CoA ligase (A0A5F5PV09) and ADP/ATP translocase (F7DPW3) highlights enhanced ATP/ADP exchange and fatty acid metabolism, promoting energy availability crucial for fibroblast activation, migration, and matrix synthesis (Table S2).

The upregulation of these proteins may reflect the fact that both FBS and A-PRF + stimulate cell proliferation, migration, and cytoskeletal reorganization, although PRF is more focused on long-term tissue repair and healing, while FBS is more oriented toward promoting rapid cell division.

In cluster 3, proteins involved in cell adhesion, cytoskeletal organization, extracellular matrix interactions, and receptor-ligand signalling pathways were downregulated only in the FBS 20% treatment compared to the control, while in the A-PRF + treatment, these proteins remained stable or even increased. This finding suggests that FBS, while promoting cell proliferation and migration, may reduce the adhesion of cells to the ECM to facilitate faster migration. Proteins such as vinculin, which play a crucial role in cell–matrix adhesion, and actin alpha-muscle, involved in cytoskeletal stability, were affected in this way<sup>63–65</sup>. In contrast, A-PRF + is likely to induce a more controlled migration where cells are encouraged to move but simultaneously stabilize their matrix and cytoskeleton for long-term tissue repair. A-PRF + contains growth factors that promote tissue regeneration and encourage fibroblasts to build a more stable ECM and to reorganize their cytoskeleton for wound healing. Therefore, the suppression of these pathways in FBS-treated cells may reflect a transient shift toward promoting rapid proliferation and migration, potentially at the expense of more stable tissue organization and long-term remodelling, which are processes more characteristic of A-PRF + activity.

In cluster 4, a strong upregulation of proteins was observed only in the A-PRF + treatment compared to the control. This suggests that A-PRF + has a unique effect on proteins involved in fructose biphosphate aldolase activity, fructose binding, and vinculin binding. These functions indicate a prominent role in energy metabolism, particularly glycolysis, as well as cytoskeletal interactions critical for cellular adhesion and structural organization. Their upregulation suggests that A-PRF + enhances cellular processes that are critical for tissue repair and matrix remodelling. In fact, glycolysis upregulation may serve to meet the increased energy demands required for processes such as extracellular matrix remodelling and cytoskeletal reorganization, which are essential for effective tissue regeneration<sup>66–68</sup>.

The increase in proteins related to adhesion and actin filament binding suggests that the PRF treatment promotes cytoskeletal organization and cellular stability, which is essential for fibroblasts during the process of tissue repair. These findings suggest that PRF induces a controlled remodelling of the cytoskeleton and matrix, contributing to a more stable, long-lasting tissue regeneration process, contrasting with the transient proliferative effects typically observed with FBS.

In cluster 5, a downregulation of proteins was observed in both the A-PRF + and FBS 20% treatments compared to the control. These proteins are involved in processes related to cell death regulation and pattern recognition (e.g., caspase binding, death receptor binding, and roundabout binding).

The suppression of Trans-2-enoyl-CoA reductase pathway components, such as U4/U6 small nuclear ribonucleoprotein Prp3-like protein (K9KCQ3) and ribonucleoprotein 4B (A0A5F5PUA5), suggests a reduced reliance on RNA splicing processes, potentially favouring a more efficient fibroblast activation state. Additionally, the downregulation of trans-2-enoyl-CoA reductase activity, a key enzyme in fatty acid  $\beta$ -oxidation, suggests a reduced reliance on lipid metabolism as an energy source in these conditions<sup>69</sup>. This could indicate a shift toward alternative metabolic pathways, such as glycolysis (upregulated in cluster 4), to meet the cellular energy demands more efficiently during regeneration or remodelling processes.

Downregulation of NADH:ubiquinone oxidoreductase subunit S6 (F6XVS1), involved in mitochondrial oxidative phosphorylation, indicates a metabolic shift that may favour glycolysis, supporting fibroblast proliferation and migration during regeneration.

The Chromatin Insulator Sequence Binding pathway, represented by the CCCTC-binding factor (F6V9V7), is also downregulated, suggesting a reorganization of chromatin accessibility that could influence gene expression patterns linked to fibroblast activation. Similarly, the downregulation of DNA helicase suggests a lower demand for DNA repair processes, potentially due to a more controlled cellular environment with reduced genotoxic stress.

The downregulation of Erlin-2 (F6S8T9) suggests a reduction in ER stress, which plays a key role in regulating cell death pathways. Additionally, the downregulation of Toll-like receptor 8 (A8QM58), a key player in immune signalling and cell death, further supports a reduced pro-apoptotic signalling environment, promoting a regenerative cellular state<sup>70–72</sup> (Table S5).

The downregulation of these proteins suggests that both FBS and PRF may suppress certain aspects of the apoptotic pathways, possibly reflecting the cells shift towards a more proliferative and regenerative state rather than undergoing cell death.

By separating the data into clusters, we identified specific trends and patterns in protein modulation, providing a clearer understanding of the biological processes and associated functional pathways.

In summary, this study provides new insights into the effects of A-PRF + secretome on primary equine fibroblasts, highlighting its impact on oxidative stress, organelle function, and metabolic reprogramming, key features of activated fibroblasts in tissue repair. The secretome-based approach was necessary due to the technical limitations of applying the fibrin clot directly to monolayer cultures, which led to mechanical disruption. Although this in vitro setting does not fully reproduce in vivo conditions, it enabled a controlled analysis of A-PRF + effects at the cellular level. While similar biologics such as PRP and mesenchymal stem cells have been tested in equine clinical trials, there were no prior in vitro studies on these products, making this investigation the first in vitro analysis of A-PRF + on equine fibroblasts. Proteomic analysis revealed significant modulation of proteins involved in metabolism, cytoskeletal organization, and extracellular matrix remodelling, supporting

A-PRF + role in tissue regeneration. However, the exact molecular mechanisms behind these changes remain unclear. Future studies should focus on further elucidating the signaling pathways involved, particularly those related to metabolic reprogramming and immune response, to better understand how A-PRF + supports tissue repair at the molecular level.

## Materials and methods

### Animals and sample collection

Samples were collected immediately prior the sacrifice of two Standardbred female horses, aged 16 and 21 years, in a certified slaughterhouse. An area at the base of the neck was clipped, and a sterile scrub was performed. Subsequently, 5 cm<sup>2</sup> biopsy of skin and subcutaneous tissue was harvested. The samples, which did not show any macroscopic abnormalities, were placed in a 50-mL Falcon tube (352,070, Fisher Scientific Oy—Ratastie 2, 01,620 Vantaa—Finland) with sterile saline solution and transported to the laboratory within an hour, similarly to what was reported by Broeckx and colleagues<sup>73</sup>. All experimental protocols and methods were reviewed and approved by the Ethical Animal Care and Use Committee of the University of Naples Federico II (OPBA—protocol number PG/2022/0,119,337). All methods were carried out in accordance with relevant guidelines and regulations. All procedures were conducted in full compliance with the ARRIVE guidelines.

### A-PRF + preparation

Whole blood was sampled from the left jugular vein of the two mares just before the sacrifice using a vacutainer system (BD Vacutainer Safety-Lok-Blood Collection Set 21Gx3/3" × 7", Becton Dickinson and Company) and collected in eight 10-mL sterile glass tubes without anticoagulants (A-PRF tubes Process for PRF™, Nice, France; Mectron, Cologne, Germany), four for each animal. Each glass tube was centrifuged within 2 min of sampling using a horizontal centrifuge (ALC 4218 Centrifuge, ALC International, Cologno Monzese, Milan, Italy). Tubes were centrifuged at 1300 rpm for 8 min for production of A-PRF +, as previously described<sup>74</sup>. At the end of the centrifugation process, the tubes were carefully placed in a portable cooler at 4 °C and transported to the laboratory within an hour.

### Preparation of the A-PRF + conditioned medium

Conditioned medium was prepared using A-PRF + clots obtained as described in the previous paragraph. Each clot was placed in a conical sterile polypropylene centrifuge tube containing 10 mL of DMEM without fetal bovine serum (FBS) and incubated for 3 days at 37 °C on a plate shaker. After incubation, the conditioned medium was centrifuged (100 g, 5 min), collected and used for secretome analysis. In preparation for the secretome analysis, the conditioned medium was aliquoted and stored at −80 °C. The control samples were processed and stored in the same manner to ensure consistency across all experimental conditions. For all cell treatments, the conditioned medium was diluted 1:4 with DMEM. As controls, cells were cultured in DMEM without FBS as a negative control and in DMEM supplemented with 20% FBS as a positive control.

### Establishment and propagation of horse fibroblast primary cells

Skin biopsies were processed immediately prior being received, to isolate primary fibroblasts. Under sterile conditions, the biopsies were transferred to a sterile culture dish and washed with sterile PBS, and adipose tissue and blood vessels were removed. The samples were then cut into fragments of approximately 1 mm<sup>3</sup> with a scalpel. The fragments were placed in a sealed tube containing collagenase I (#C9891, Sigma Aldrich, 2 mg/mL, in DMEM with 20% FBS) for 4 h at 37 °C, then centrifuged at 1600 g for 10 min. The supernatant was discarded, and the pellet was resuspended in DMEM with 20% FBS, 2 mM L-glutamine, 100 U/mL penicillin, 0.1 mg/mL streptomycin and 2.5 µg/mL amphotericin B, and plated in culture dish. Cells were routinely grown in culture dishes (Corning, Corning, New York) in an environment containing 5% CO<sub>2</sub> at 37 °C and split every 2 days using a solution of 0.5% trypsin and 0.2% EDTA. Fibroblasts, after isolation from skin biopsies, derived exclusively from the two previously mentioned horses were expanded in culture until passage 3, at which point they were cryopreserved in a freezing solution consisting of 90% FBS and 10% DMSO. For all experiments, fibroblasts were thawed and used between passages 3 and 7. Cell growth and viability were monitored using phase-contrast microscopy and trypan blue staining<sup>74,75</sup>. The cells were frozen in a freezing container that provides a cooling rate of 1 °C per minute, kept at −80 °C overnight, and transferred in liquid nitrogen for long term storage<sup>76,77</sup>. Each treatment and analysis was performed in at least three independent experiments. Specifically, each assay was conducted three times on fibroblasts derived from both horses, each treated with their corresponding autologous A-PRF +. The resulting data were then averaged to obtain representative values reflecting the effects of the two types of A-PRF + used. For each experiment, fibroblasts from both horses were treated with their corresponding autologous A-PRF +, and results were averaged. In particular, for each assay involving image-based analysis, at least three distinct microscopic fields containing different cells were acquired and analyzed for each experimental condition. These fields were selected from three different wells within the same multiwell plate, representing technical replicates. The values obtained from the three fields were averaged to obtain a single representative value per condition, in accordance with standard in vitro procedures.

### Cellular metabolic activity assay

Cell metabolic activity was established by measuring mitochondrial metabolic activity using MTT (3-(4,5-Dimethylthiazol-2-yl)-2,5-diphenyltetrazolium bromide) assay as previously reported<sup>78</sup>. Fibroblasts (8 × 10<sup>3</sup> cells/well) were plated into 96-well plates for 24 h, then A-PRF + conditioned medium was added for 24 h. Afterward, MTT assay at 0.5 mg/mL final concentration for 4 h was added. The absorbance was measured at 570 nm using a microplate reader (Multiskan Go, Thermo Scientific, Waltham, MA, USA). Cell metabolic activity was expressed as a percentage relative to the untreated cells cultured in medium without FBS and set to

100% metabolic activity, whereas 10% DMSO was used as negative control and set to 0% of metabolic activity. Cells treated with medium containing 20% FBS were used as positive control of metabolic activity.

### Mitochondrial membrane potential determination

Mitochondrial membrane potential was measured using tetramethylrhodamine ethyl ester (TMRE) (Invitrogen, Burlington, ON, Canada)<sup>79</sup>. After growing fibroblasts at  $8 \times 10^3$  per well, the cells were treated with A-PRF + conditioned medium for 24 h. DMEM without FBS and with 20% FBS were used as negative and positive control, respectively. The cells were then washed with PBS and incubated with 100 nM TMRE in DMEM without phenol red and FBS for 30 min at 37 °C in the dark. Excess dye was then removed by washing with PBS and fluorescence was measured using a PerkinElmer EnSpire multimode plate reader (excitation/emission 549 nm/574 nm). The quantitative analysis is reported as fluorescence intensity and compared to the relative controls. The fluorescence representative images of live cells were captured using a ZOE Fluorescence Imager (Bio-Rad, Mississauga, ON, Canada).

### Mitochondrial morphology analysis

Fibroblasts were seeded ( $3 \times 10^4$  cells/well) in 12-well plates allowing to adhere for 24 h. After, treated cells were incubated for 24 h with A-PRF + conditioned medium. Negative control cells were incubated with DMEM without FBS, while positive control cells were incubated with DMEM 20% FBS. For mitochondria staining, after the treatment, the medium was removed; thus, the cells seeded on glass coverslips were incubated for 30 min at 37 °C in a serum-free medium containing 200 nM Mitotracker Red CMXRos (Invitrogen-Molecular Probes, Waltham, MA, USA). Coverslips were fixed in PBS-4% paraformaldehyde, and then permeabilized in cold acetone for 5 min on ice. After, quenching in PBS containing 1% BSA and 50 mM  $\text{NH}_4\text{Cl}$  was performed<sup>80</sup>.

Nuclei were counterstained with 1.6  $\mu\text{M}$  Hoechst 33,342 (Sigma Aldrich, St. Louis, MO, USA) for 10 min. Images were acquired on a laser scanning confocal microscope (TCS SP8; Leica Microsystems) equipped with a plan Apo 63X, NA 1.4 oil immersion objective lens. Quantitative analyses to determine mitochondrial fusion/fragmentation were performed by the ImageJ program, version 1.47 ( $N \geq 10$ ).

### Clonogenic potential determination

The clonogenic potential was assessed as reported<sup>81</sup>. A-PRF + conditioned medium was used to stimulate equine fibroblasts, while DMEM without serum and containing 20% FBS were used as negative and positive control, respectively. Cells were seeded in 6-well plates at a seeding density of  $1 \times 10^4$  cells/well. After incubation for 4 days, the culture was terminated by removing the medium and washing the colonies twice with PBS. The cells were fixed and stained with a solution containing 3.7% formaldehyde and 0.5% crystal violet for 30 min, and then washed twice with PBS. Images were obtained and the clonogenic potential was determined from a 1% SDS cell dissolution and measured by using a spectrophotometer at 570 nm (Multiskan Go, Thermo Scientific, Waltham, MA, USA).

### Wound healing assay

In the wound healing analysis,  $5 \times 10^5$  cells were seeded in 24-well plates and then incubated at 37 °C for 24 h. After that, a linear scratch was created with a 10  $\mu\text{L}$  sterile pipette tip at the center of the cell monolayer. Cells were washed with PBS and cultured in A-PRF + conditioned medium for 24 h. DMEM without FBS and containing 20% FBS were used in negative and positive controls, respectively. Different fields were analysed by contrast-phase microscopy, and each scratch area was photographed at 0 and 24 h. Images were obtained, and the wound size area (%) was calculated using ImageJ, version 1.47<sup>82</sup>.

### Evaluation of cell cycle re-entry

To determine the cell cycle phases analysis, cells ( $4.5 \times 10^4$  cells/well) were seeded into 24-well plates. To induce cell cycle exit, fibroblasts were starved for 24 h in DMEM without FBS. After starvation, control cells were maintained in DMEM without FBS, while the treatment group was exposed to A-PRF + conditioned medium. Positive control cells were treated with DMEM containing 20% FBS to promote cell cycle re-entry. After 24 h of treatment, cells were detached, centrifuged, and the resulting pellets were resuspended in a hypotonic lysis solution containing 50  $\mu\text{g/mL}$  propidium iodide, 0.1% (w/v) sodium citrate, and 0.1% Triton X-100. After incubation at 4 °C for 30 min, cells were analyzed by a Becton Dickinson FACScan flow cytometer, using the Cell Quest software version 4<sup>83,84</sup>. Cellular debris was excluded from the analysis by raising the forward scatter threshold, then the percentage of cells in G1, G2 and S phase were calculated.

### Reactive oxygen species quantification

Reactive oxygen species levels were measured by using 10  $\mu\text{M}$  6-carboxy-2',7'-dichlorodihydrofluorescein diacetate (DCFH-DA, Sigma Aldrich, St. Louis, MO, USA)<sup>85</sup>. Fibroblast primary cells were seeded ( $8 \times 10^4$  cells/well) in a black 96-well ViewPlate (PerkinElmer, Waltham, MA, USA), allowing them to adhere for 24 h. Next, the cells were incubated for 3, 6 and 24 h with A-PRF + conditioned medium. DMEM without FBS and containing 20% FBS were used as negative and positive control, respectively. After washing, a staining solution containing DCFH-DA in serum-free medium without phenol red was added for 20 min at 37 °C in the dark. The stained cells were washed, and representative images were acquired using a ZOE Fluorescent Cell Imaging System (Magnification, 20 $\times$ ). The fluorescence signals (excitation/emission 485 nm/535 nm) were read using a PerkinElmer EnSpire multimode plate reader and expressed as DCFH fluorescence intensity.

### Autophagy determination

To detect the typical structures for autophagy, such as acidic vesicular organelles (AVOs), acridine orange (AO; Sigma Aldrich, St. Louis, MO, USA) was used. Fibroblasts ( $8 \times 10^3$  cells/well) were plated into 96-well plates for 24 h, then A-PRF + conditioned medium was added for 24 h. DMEM without FBS and containing 20% FBS were used as negative and positive control, respectively<sup>86</sup>.

After washing, a staining solution containing 2  $\mu$ g/ml AO in serum-free medium without phenol red was added for 20 min at 37 °C in the dark. The stained cells were washed, and representative images were acquired using a ZOE Fluorescent Cell Imaging System (Magnification, 20 $\times$ ). The fluorescence signals (excitation/emission 480 nm/525 and 650 nm) were read using a PerkinElmer EnSpire multimode plate reader. The values were expressed as the ratio of the two AO fluorescence signals.

### Endoplasmic reticulum expansion evaluation

The intensity of endoplasmic reticulum (ER)-specific fluorescence, indicating ER expansion, which is characteristic of activated endoplasmic reticulum stress, was measured using the ER-ID Red analysis kit (Enzo Life Science, Farmingdale, NY, USA)<sup>87</sup>. Fibroblasts ( $8 \times 10^3$  cells/well) were plated into 96-well plates for 24 h, then A-PRF + conditioned medium was added for 24 h. DMEM without FBS and containing 20% FBS were used as negative and positive control, respectively. After incubation, 100  $\mu$ L of 1X assay buffer with 1  $\mu$ L of ER-ID Red detection reagent and 1  $\mu$ L of Hoechst 33,342 nuclear dye was added to each well and the cells were incubated for 20 min at 37 °C. The stained cells were washed, and representative images were acquired using a ZOE Fluorescent Cell Imaging System (Magnification, 20 $\times$ ). The fluorescence signals (ER-ID: excitation/emission 560 nm/630 nm) were read using a PerkinElmer EnSpire multimode plate reader.

### Collagen type I determination

Fibroblasts were seeded ( $5 \times 10^4$  cells/well) in 24-well plates containing glass cover slips allowing them to adhere for 24 h. Then, cells were cultured in A-PRF + conditioned medium for 48 h. DMEM without FBS and containing 20% FBS were used in negative and positive controls, respectively.

After treatments, cells were washed in PBS, fixed in PBS-4% paraformaldehyde and permeabilized 5 min in PBS containing 0.2% triton. A blocking solution containing PBS-1% BSA and 50 mM  $\text{NH}_4\text{Cl}$  for 20 min was added to each well. Thereafter, cells were stained with Phalloidin-Tetra-methyl-rhodamine B isothiocyanate (Merk, Darmstadt, Germany) for 20 min to visualize actin filaments<sup>88</sup>.

The immunostaining was performed for 1 h at room temperature with the rabbit polyclonal anti-collagen I (Novus Biologicals, Bio-Techne, Minneapolis, Minnesota, USA). Alexa fluor 488 antibody (Molecular Probes, Invitrogen, Waltham, Massachusetts, USA) was used as secondary antibody and incubated for 45 min. Nuclei were counterstained with 1.6  $\mu$ M Hoechst 33,342 (Sigma Aldrich, St. Louis, MO, USA) for 10 min. Images were acquired on a laser scanning confocal microscope (TCS SP8; Leica Microsystems) equipped with a plan Apo 63X, NA 1.4 oil immersion objective lens. Quantitative analyses were performed by the ImageJ program, version 1.47 ( $N \geq 10$ ).

### Enzyme-linked immunosorbent assay (ELISA)

Fibroblasts ( $3 \times 10^4$  cells/well) were plated into 24-well plates for 24 h, then A-PRF + conditioned medium was added for 24 h. Quantitative measurement of released proteins was assessed by commercially available enzyme-linked immunosorbent assay (ELISA). Then supernatants were collected and analysed according to the instructions of the immunoassay kit (equine TGF $\beta$ 1 ELISA Kit; equine VEGF-A ELISA Kit; equine PDGF-BB ELISAkit; MyBioSource, Inc., San Diego, CA, USA).

### RNA extraction, reverse transcription, and real-time PCR

Total RNA was isolated from treated cells after 24 h using Trizol reagent (Gibco, Thermo Fisher Scientific), according to manufacturer's instructions. Aliquots of total RNA for Real-time PCR test were subjected to DNase I digestion (Thermo Fisher Scientific) and reverse transcribed using M-MLV Reverse Transcriptase (Thermo Fisher Scientific) according to the manufacturer's protocol. Thermal conditions for reverse transcription were 25 °C for 10 min, 37 °C for 50 min, and 75 °C for 15 min. In the last step, RNase H was added.

Real-time PCR was performed with LightCycler<sup>®</sup> 480 System (La Roche Ltd) using SYBR Green detection in a total volume of 20  $\mu$ L with 1  $\mu$ L of forward and reverse primers (5  $\mu$ M) and 10  $\mu$ L of PowerUp<sup>™</sup> SYBR<sup>™</sup> Green Master Mix (Thermo Fisher Scientific). Values were determined from standard curve generated from serial cDNA dilutions and normalized to GAPDH.

The primers used for the real-time PCR reactions are listed in the table below.

The  $2^{-\Delta\Delta\text{CT}}$  method was used to analyse the results and relative mRNA expression levels were determined as fold-induction relative to Ctrl cells, set as 1<sup>89</sup>.

Primer sequence (5'-3')		
Target gene	Forward	Reverse
MT1-MMP	TAARCCCAAAAACCCRCCTATG	TCCTCACCCGCCAGAACCA
MMP2	ATGGCGCCCATTTACACGTA	AGCTCTGAATGCCCTTGATG
MMP9	TGCAACGTGGACATCTTCGA	CCCTCCAAGAGTCGCCAGTA
IL-6	AGCAAGTGTGAAAACAGCAAG	CATCAGGCAGGTCTCCTGAT
IL-8	TTCCAAGCTGGCTGTTGCT	TGATACAACCGCAGCTTCACA
IL-10	TTCAGCAGGGTGAAGACTTTC	CTTGCAACCCAGGTAACCTTA

Primer sequence (5'-3')		
Target gene	Forward	Reverse
EGFR	TGGACTCATGGACTGGTTTGGC	TGGATCAACTCAGTCAGCAAG
FGF2	GAACCGTTATCTTGCTATGAAGG	CCAACTGGAGTATTTCCTTGAC
TGF- $\beta$ 1	CCGAGAGAGCGCTGAGA	ATAGATTTCGTTTTCCTTTTC

## Proteomics

### *Proteome extraction from A-PRF + clot*

The platelet-rich fibrin was collected as previously described. For the proteome extraction, the first step involved homogenizing the sample using 3 cycles of mechanical agitation, each lasting 30 s at 500 rpm with beads. The sample was subsequently sonicated with 15 on/off cycles of 30 s each. Concerning A-PRF + sample preparation, three different strategies were used, non-depleted, depletion with perchloric acid, and depletion through the iST-ENRICH kit from PreOmics (PreOmics, Martinsried, Germany) was used according to the manufacturer's instructions. Undepleted samples were lysed and digested as reported elsewhere<sup>90</sup>. Depletion with perchloric acid and subsequent digestion was performed as reported previously<sup>91</sup>. For each sample preparation method, 20  $\mu$ L of A-PRF + were subjected to digestion. Secretome and fibroblast were digested as reported elsewhere<sup>90</sup>. iST-ENRICH results were finally selected (data not shown).

### *Proteome extraction from secretome A-PRF + and treated fibroblast*

The secretome analyses were performed on the conditioned medium, prepared according to the previously described protocol. Proteomic analysis of fibroblasts was conducted after 24 h of treatment with A-PRF + conditioned medium. The samples were initially resuspended in 150  $\mu$ L of 50 mM ammonium bicarbonate and subjected to ultrasonic sonication for 20 min to promote cell lysis and protein extraction. Subsequently, protein quantification was performed using the Bicinchoninic Acid (BCA) Assay Kit (Thermo Fisher Scientific, Waltham, MA, USA), following the manufacturer's instructions. After quantification, the proteins were reduced and alkylated using dithiothreitol (DTT, 10 mM) and iodoacetamide (IAA, 20 mM). Enzymatic digestion was carried out by incubating overnight at 37 °C with trypsin at an enzyme-to-substrate ratio of 1:100. Finally, a cleanup step was performed on the samples using a reverse-phase SPE cartridge (Strata-X, Phenomenex, Bologna, Italy).

### *Proteomics analysis by nLC-HRMS/MS*

All analyses were carried out using a label-free quantification (LFQ) approach. Sample preparation involved resuspending both perchloric acid-depleted and non-depleted specimens in 100  $\mu$ L of a solution composed of 95% LC-MS grade water and 5% LC-MS grade acetonitrile, plus 0.1% trifluoroacetic acid (TFA). The analyses were conducted on a Thermo Scientific Ultimate 3000 nano-LC system connected to an Orbitrap Fusion Lumos mass spectrometer (Thermo Scientific, Bremen) fitted with a nano-electrospray ionization (EasySpray, Thermo)) source.

The chromatographic separation utilized solvent A (LC-MS grade water containing 0.1% formic acid) and solvent B (a mix of 80% acetonitrile and 20% water, LC-MS grade, with 0.08% formic acid). Peptides were first captured on a trap column for concentration before being resolved on a PepMap C18 analytical column (75  $\mu$ m  $\times$  250 mm, 2  $\mu$ m particle size, 100 Å pore size, Thermo Scientific) at a flow rate of 0.3  $\mu$ L/min across a 60-min gradient. The gradient of solvent B was programmed as follows: an initial 4% rising to 35% over 40 min, followed by a ramp to 99% within 2 min, reduced back to 4% over 5 min, and maintained at that level until the run concluded.

For A-PRF + samples, data were acquired in Data-Independent Acquisition (DIA) mode. The full MS scan was performed in the m/z range of 400–1000 with a resolution of 60,000 in positive ion mode. Fragmentation for MS2 was executed using Higher-energy Collisional Dissociation (HCD) with a resolution of 30,000. For further acquisition parameters, refer to<sup>92</sup>.

The same nano-LC-HRMS setup was employed for proteomic evaluation of both the secretome and fibroblast samples, although in these cases, Data-Dependent Acquisition (DDA) mode was used. MS1 scans were acquired in the 375–1500 m/z range at 120,000 resolution. Automatic Gain Control (AGC) targets and ion injection times were set to default (standard and auto, respectively), using quadrupole-based isolation. MS/MS scans were performed in the Orbitrap at 15,000 resolution. Ions with undetermined charge or singly charged species were excluded from fragmentation. A normalized isolation window of 1.6 Da was applied, and HCD was used for fragmentation with a collision energy of 30. The injection time for MS/MS was set to a maximum of 50 ms, with standard AGC settings. Dynamic exclusion was enabled with a 30-s duration.

### *Proteomics data analysis*

A-PRF + DIA data were processed using DIA-NN v 1.9, a FDR threshold of 1% was used, library-free search was enabled and all other parameters were left by default setting. DDA data analysis for Secretome and Fibroblast were processed using Proteome Discoverer v 2.5.0.400, for both with a false discovery rate of 1%, was used. Data were normalized by median, log-transformed and autoscaled prior statistical analysis. Subsequently, identified proteins were analyzed for functional enrichment using STRING and ShinyGO to determine key biological signaling pathways and protein–protein interactions.

## Statistical analysis

Data was assessed for normality with Shapiro–Wilk test and reported as mean  $\pm$  SD of the results from three independent experiments. Statistical analysis was performed using an analysis of variance test (ANOVA), and multiple comparisons were made with the post-hoc Bonferroni test using GraphPad Prism 8.0 software (San Diego, CA, USA). Significance was assumed at  $p < 0.05$ .

## Conclusions

The molecular mechanisms underlying A-PRF + regenerative potential remain limited, and this study provides new insights into its effects on equine primary fibroblasts.

The combination of secretome analysis, in vitro experiments, and proteomic profiling has provided a comprehensive understanding of the molecular and cellular effects of A-PRF +. Secretome analysis revealed a broad array of proteins involved in extracellular matrix remodelling, metabolic regulation, and cytoskeletal organization, highlighting PRF potential for long-term regenerative processes. This was further corroborated by in vitro experiments, including MTT, clonogenic assays, and cell cycle analysis, which demonstrated PRF ability to enhance fibroblast viability, migration, and proliferation. Additionally, ROS production and mitochondrial activity, assessed through increased oxidative stress and mitochondrial fragmentation, as well as ER and lysosomal expansion, showed a significant response to A-PRF +, aligning with the proteomic data that suggested a reprogramming of cellular metabolism and stress adaptation mechanisms.

In conclusion, the proteomic analysis revealed distinct molecular signatures associated with A-PRF + and FBS treatments, highlighting their divergent effects on fibroblast biology. While both treatments modulate key metabolic and signalling pathways, it is hypothesized that PRF specifically promotes long-term tissue regeneration through metabolic reprogramming and cytoskeletal stabilization, in contrast to FBS, which may focus more on rapid cell proliferation and migration. These insights provide a deeper understanding of PRF regenerative biochemical potential and its advantages in equine regenerative medicine.

## Data availability

Data is provided within the manuscript or supplementary information files.

Received: 20 March 2025; Accepted: 8 May 2025

Published online: 23 May 2025

## References

- Naik, B., Karunakar, P., Jayadev, M. & Marshal, V. R. Role of Platelet rich fibrin in wound healing: A critical review. *J. Conserv. Dent.* **16**, 284–293. <https://doi.org/10.4103/0972-0707.114344> (2013).
- Buonocore, M. et al. Exploiting the features of short peptides to recognize specific cell surface markers. *Int. J. Mol. Sci.* **24**, 15610. <https://doi.org/10.3390/ijms242115610> (2023).
- Song, P., He, D., Ren, S., Fan, L. & Sun, J. Platelet-rich fibrin in dentistry. *J. Appl. Biomater. Funct. Mater.* <https://doi.org/10.1177/22808000241299588> (2024).
- Crisci, A. et al. Standardized protocol proposed for clinical use of L-PRF and the use of L-PRF Wound Box\*. *J. Unexplored Med. Data.* **2**, 77–87. <https://doi.org/10.20517/2572-8180.2017.17> (2017).
- Masuki, H. et al. Growth factor and pro-inflammatory cytokine contents in platelet-rich plasma (PRP), plasma rich in growth factors (PRGF), advanced platelet-rich fibrin (A-PRF), and concentrated growth factors (CGF). *Int. J. Implant Dent.* **2**, 19. <https://doi.org/10.1186/s40729-016-0052-4> (2016).
- Pavlovic, V., Ciric, M., Jovanovic, V., Trandafilovic, M. & Stojanovic, P. Platelet-rich fibrin: Basics of biological actions and protocol modifications. *Open Med. (Wars)* **16**, 446–454. <https://doi.org/10.1515/med-2021-0259> (2021).
- Narayanaswamy, R. et al. Evolution and clinical advances of platelet-rich fibrin in musculoskeletal regeneration. *Bioengineering* **10**, 58. <https://doi.org/10.3390/bioengineering10010058> (2023).
- Stefanescu, A. et al. Assessing the effectiveness of A-PRF+ for treating periodontal defects: A prospective interventional pilot study involving smokers. *Medicina* **60**, 1897. <https://doi.org/10.3390/medicina60111897> (2024).
- Pitzurra, L., Jansen, I. D. C., de Vries, T. J., Hoogenkamp, M. A. & Loos, B. G. Effects of L-PRF and A-PRF+ on periodontal fibroblasts in in vitro wound healing experiments. *J. Periodontal. Res.* **55**, 287–295. <https://doi.org/10.1111/jre.12714> (2020).
- Santos Pereira, V. B., Barbirato, D. D. S., Lago, C. A. P. D. & Vasconcelos, B. C. D. E. The effect of advanced platelet-rich fibrin in tissue regeneration in reconstructive and graft surgery: Systematic review. *J. Craniofac. Surg.* **34**, 1217–1221. <https://doi.org/10.1097/SCS.00000000000009328> (2023).
- Liu, Y. H. et al. Advanced platelet-rich fibrin (A-PRF) has an impact on the initial healing of gingival regeneration after tooth extraction. *J. Oral Biosci.* **64**, 141–147. <https://doi.org/10.1016/j.job.2021.11.001> (2022).
- Kosmidis, K., Ehsan, K., Pitzurra, L., Loos, B. & Jansen, I. An in vitro study into three different PRF preparations for osteogenesis potential. *J. Periodontal. Res.* **58**, 483–492. <https://doi.org/10.1111/jre.13116> (2023).
- Ghanaati, S. et al. Advanced platelet-rich fibrin: A new concept for cell-based tissue engineering by means of inflammatory cells. *J. Oral Implantol.* **40**, 679–689. <https://doi.org/10.1563/aaid-joi-D-14-00138> (2014).
- Caston, S. S. Wound care in horses. *Vet. Clin. N. Am. Equine Pract.* **28**, 83–100. <https://doi.org/10.1016/j.cveq.2012.01.001> (2012).
- Spink, J. & Moyer, D. C. Defining the public health threat of food fraud. *J. Food Sci.* **76**, R157–R163. <https://doi.org/10.1111/j.1750-3841.2011.02417.x> (2011).
- Wang, X., Yang, Y., Zhang, Y. & Miron, R. J. Fluid platelet-rich fibrin stimulates greater dermal skin fibroblast cell migration, proliferation, and collagen synthesis when compared to platelet-rich plasma. *J. Cosmet. Dermatol.* **18**, 2004–2010. <https://doi.org/10.1111/jocd.12955> (2019).
- Dachlan, I. et al. The effect of platelet-rich fibrin on normal dermal fibroblast proliferation after mitomycin-c treatment: An in vitro study. *Ann. Med. Surg. (Lond.)* **62**, 473–476. <https://doi.org/10.1016/j.amsu.2021.01.093> (2021).
- Marescal, O. & Cheeseman, I. M. Cellular mechanisms and regulation of quiescence. *Dev. Cell* **55**, 259–271. <https://doi.org/10.1016/j.devcel.2020.09.029> (2020).
- Pagliara, V. et al. Myogenesis in C2C12 cells requires phosphorylation of ATF6a by p38 MAPK. *Biomedicine* **11**, 1457. <https://doi.org/10.3390/biomedicine11051457> (2023).
- Matsuzaki, S. et al. Physiological ER stress mediates the differentiation of fibroblasts. *PLoS ONE* **10**, e0123578. <https://doi.org/10.1371/journal.pone.0123578> (2015).

21. Miron, R. J. et al. Injectable platelet rich fibrin (i-PRF): Opportunities in regenerative dentistry?. *Clin. Oral Investig.* **21**, 2619–2627. <https://doi.org/10.1007/s00784-017-2063-9> (2017).
22. Farooq, M., Khan, A. W., Kim, M. S. & Choi, S. The role of fibroblast growth factor (FGF) signaling in tissue repair and regeneration. *Cells* **10**, 3242. <https://doi.org/10.3390/cells10113242> (2021).
23. Kajanne, R. et al. EGF-R regulates MMP function in fibroblasts through MAPK and AP-1 pathways. *J. Cell Physiol.* **212**, 489–497. <https://doi.org/10.1002/jcp.21041> (2007).
24. Ruangpanit, N. et al. Gelatinase A (MMP-2) activation by skin fibroblasts: Dependence on MT1-MMP expression and fibrillar collagen form. *Matrix Biol.* **20**, 193–203. [https://doi.org/10.1016/S0945-053X\(01\)00135-4](https://doi.org/10.1016/S0945-053X(01)00135-4) (2001).
25. Johnson, B. Z., Stevenson, A. W., Prêle, C. M., Fear, M. W. & Wood, F. M. The role of IL-6 in skin fibrosis and cutaneous wound healing. *Biomedicines* **8**, 101. <https://doi.org/10.3390/biomedicines8050101> (2020).
26. Balaji, S. et al. Interleukin-10-mediated regenerative postnatal tissue repair is dependent on regulation of hyaluronan metabolism via fibroblast-specific STAT3 signaling. *FASEB J.* **31**, 868–881. <https://doi.org/10.1096/fj.201600856R> (2017).
27. Li, Y. et al. HB-EGF-induced IL-8 secretion from airway epithelium leads to lung fibroblast proliferation and migration. *BMC Pulm. Med.* **21**, 347. <https://doi.org/10.1186/s12890-021-01726-w> (2021).
28. Hamill, K. J. et al. Alpha actinin-1 regulates cell-matrix adhesion organization in keratinocytes: Consequences for skin cell motility. *J. Invest. Dermatol.* **135**, 1043–1052. <https://doi.org/10.1038/jid.2014.505> (2015).
29. Dias, H. B., de Oliveira, J. R., Donadio, M. V. F. & Kimura, S. Fructose-1,6-bisphosphate prevents pulmonary fibrosis by regulating extracellular matrix deposition and inducing phenotype reversal of lung myofibroblasts. *PLoS ONE* **14**, e0222202. <https://doi.org/10.1371/journal.pone.0222202> (2019).
30. Liang, Z. H. et al. GLI family zinc finger protein 2 promotes skin fibroblast proliferation and DNA damage repair by targeting the miR-200/ataxia telangiectasia mutated axis in diabetic wound healing. *Kaohsiung J. Med. Sci.* **40**, 422–434. <https://doi.org/10.1002/kjm2.12813> (2024).
31. Kwon, Y. YAP/TAZ as molecular targets in skeletal muscle atrophy and osteoporosis. *Aging Dis.* **16**, 299–320. <https://doi.org/10.14336/AD.2024.0306> (2024).
32. Manganelli, V. et al. Role of ERLINs in the control of cell fate through lipid rafts. *Cells* **10**, 2408. <https://doi.org/10.3390/cells10092408> (2021).
33. Soares, C. S., Babo, P. S., Faria, S., Pires, M. A. & Carvalho, P. P. Standardized Platelet-Rich Fibrin (PRF) from canine and feline origin: An analysis on its secretome pattern and architectural structure. *Cytokine* **148**, 155695. <https://doi.org/10.1016/j.cyto.2021.155695> (2021).
34. Al-Sharabi, N. et al. Proteomic analysis of mesenchymal stromal cells secretome in comparison to leukocyte- and platelet-rich fibrin. *Int. J. Mol. Sci.* **24**, 13057. <https://doi.org/10.3390/ijms241713057> (2023).
35. Yaprak, E., Kasap, M., Akpınar, G., Islek, E. E. & Sinanoglu, A. Abundant proteins in platelet-rich fibrin and their potential contribution to wound healing: An explorative proteomics study and review of the literature. *J. Dent. Sci.* **13**, 386–395. <https://doi.org/10.1016/j.jds.2018.08.004> (2018).
36. Takaya, K., Okabe, K. & Ishigami, A. Actin cable formation and epidermis–dermis positional relationship during complete skin regeneration. *Sci. Rep.* **12**, 15913. <https://doi.org/10.1038/s41598-022-18175-y> (2022).
37. Gurtner, G. C., Werner, S., Barrandon, Y. & Longaker, M. T. Wound repair and regeneration. *Nature* **453**, 314–321. <https://doi.org/10.1038/nature07039> (2008).
38. Vondriska, T. M., Pass, J. M. & Ping, P. Scaffold proteins and assembly of multiprotein signaling complexes. *J. Mol. Cell Cardiol.* **37**, 391–397. <https://doi.org/10.1016/j.yjmcc.2004.04.021> (2004).
39. Tracy, L. E., Minasian, R. A. & Caterson, E. J. Extracellular matrix and dermal fibroblast function in the healing wound. *Adv. Wound Care* **5**(3), 119–136 (2016).
40. Jolly, L. A. et al. Fibroblast-mediated collagen remodeling within the tumor microenvironment facilitates progression of thyroid cancers driven by BrafV600E and Pten loss. *Cancer Res.* **76**, 1804–1813. <https://doi.org/10.1158/0008-5472.CAN-15-2351> (2016).
41. Engström, W., Ward, A. & Moorwood, K. The role of scaffold proteins in JNK signalling. *Cell Prolif.* **43**, 56–66. <https://doi.org/10.1111/j.1365-2184.2009.00654.x> (2010).
42. Tang, D. D. & Gerlach, B. D. The roles and regulation of the actin cytoskeleton, intermediate filaments and microtubules in smooth muscle cell migration. *Respir. Res.* **18**, 54. <https://doi.org/10.1186/s12931-017-0544-7> (2017).
43. Etienne-Manneville, S. Actin and microtubules in cell motility: Which one is in control?. *Traffic* **5**, 470–477. <https://doi.org/10.1111/j.1600-0854.2004.00196.x> (2004).
44. Nobes, C. D. & Hall, A. Rho, rac, and cdc42 GTPases regulate the assembly of multimolecular focal complexes associated with actin stress fibers, lamellipodia, and filopodia. *Cell* **81**, 53–62. [https://doi.org/10.1016/0092-8674\(95\)90370-4](https://doi.org/10.1016/0092-8674(95)90370-4) (1995).
45. Spiering, D. & Hodgson, L. Dynamics of the Rho-family small GTPases in actin regulation and motility. *Cell Adh. Migr.* **5**, 170–180. <https://doi.org/10.4161/cam.5.2.14403> (2011).
46. Ma, Y. et al. Histone demethylases in autophagy and inflammation. *Cell Commun. Signal.* **23**, 24. <https://doi.org/10.1186/s12964-024-02006-w> (2025).
47. Ulukan, B., Sila Ozkaya, Y. & Zeybel, M. Advances in the epigenetics of fibroblast biology and fibrotic diseases. *Curr. Opin. Pharmacol.* **49**, 102–109. <https://doi.org/10.1016/j.coph.2019.10.001> (2019).
48. Kirk, T., Ahmed, A. & Rognoni, E. Fibroblast memory in development, homeostasis and disease. *Cells* **10**, 2840. <https://doi.org/10.3390/cells10112840> (2021).
49. Liu, S. et al. Fetal bovine serum, an important factor affecting the reproducibility of cell experiments. *Sci. Rep.* **13**, 1942. <https://doi.org/10.1038/s41598-023-29060-7> (2023).
50. Yaneselli, K. et al. Impact of different formulations of platelet lysate on proliferative and immune profile of equine mesenchymal stromal cells. *Front. Vet. Sci.* **11**, 1410855. <https://doi.org/10.3389/fvets.2024.1410855> (2024).
51. Santos, A. & Sheguti, T. M. Platelet-rich plasma (PRP) as an alternative to fetal bovine serum (FBS) in the culture of mesenchymal stem cells in cell therapy. *J. Stem Cell Res. Ther.* **7**, 26–28. <https://doi.org/10.15406/jsrt.2022.07.00153> (2022).
52. He, L., Lin, Y., Hu, X., Zhang, Y. & Wu, H. A comparative study of platelet-rich fibrin (PRF) and platelet-rich plasma (PRP) on the effect of proliferation and differentiation of rat osteoblasts in vitro. *Oral Surg. Oral Med. Oral Pathol. Oral Radiol. Endod.* **108**, 707–713. <https://doi.org/10.1016/j.tripleo.2009.06.044> (2009).
53. Atsu, N., Ekinci-Aslanoglu, C., Kantarci-Demirkiran, B. & Nuhoglu, F. The comparison of platelet-rich plasma versus injectable platelet rich fibrin in facial skin rejuvenation. *Dermatol. Ther.* <https://doi.org/10.1155/2023/3096698> (2023).
54. Coronado, M. et al. Physiological mitochondrial fragmentation is a normal cardiac adaptation to increased energy demand. *Circ. Res.* **122**, 282–295. <https://doi.org/10.1161/CIRCRESAHA.117.310725> (2018).
55. Guo, T. et al. Mitochondrial fission and bioenergetics mediate human lung fibroblast durotaxis. *JCI Insight.* **8**, e157348. <https://doi.org/10.1172/jci.insight.157348> (2023).
56. Yu, T., Wang, L., Zhang, L. & Deuster, P. A. Mitochondrial fission as a therapeutic target for metabolic diseases: Insights into antioxidant strategies. *Antioxidants (Basel)* **12**, 1163. <https://doi.org/10.3390/antiox12061163> (2023).
57. Sterczala, B. et al. Impact of APRF+ in combination with autogenous fibroblasts on release growth factors, collagen, and proliferation and migration of gingival fibroblasts: An in vitro study. *Materials (Basel)* **15**, 796. <https://doi.org/10.3390/ma15030796> (2022).
58. Bagdadi, K. et al. Reduction of relative centrifugal forces increases growth factor release within solid platelet-rich-fibrin (PRF)-based matrices: A proof of concept of LSCC (low speed centrifugation concept). *Eur. J. Trauma Emerg. Surg.* **45**, 467–479. <https://doi.org/10.1007/s00068-017-0785-7> (2019).

59. Chen, K. et al. Regulation of inflammation by members of the formyl-peptide receptor family. *J. Autoimmun.* **85**, 64–77. <https://doi.org/10.1016/j.jaut.2017.06.012> (2017).
60. Ding, H. et al. Transferrin receptor 1 ablation in satellite cells impedes skeletal muscle regeneration through activation of ferroptosis. *J. Cachexia Sarcopenia Muscle*. **12**, 746–768. <https://doi.org/10.1002/jcsm.12700> (2021).
61. Czapiga, M., Gao, J. L., Kirk, A. & Lektrom-Himes, J. Human platelets exhibit chemotaxis using functional N-formyl peptide receptors. *Exp. Hematol.* **33**, 73–84. <https://doi.org/10.1016/j.exphem.2004.09.010> (2005).
62. Ward, J. H., Kushner, J. P. & Kaplan, J. Transferrin receptors of human fibroblasts. Analysis of receptor properties and regulation. *Biochem. J.* **208**, 19–26. <https://doi.org/10.1042/bj2080019> (1982).
63. Kanaya, S., Nemoto, E., Ebe, Y., Somerman, M. J. & Shimauchi, H. Elevated extracellular calcium increases fibroblast growth factor-2 gene and protein expression levels via a cAMP/PKA dependent pathway in cementoblasts. *Bone* **47**, 564–572. <https://doi.org/10.1016/j.bone.2010.05.042> (2010).
64. Izard, T. & Brown, D. T. Mechanisms and functions of vinculin interactions with phospholipids at cell adhesion sites. *J. Biol. Chem.* **291**, 2548–2555. <https://doi.org/10.1074/jbc.R115.686493> (2016).
65. Giannone, G. Super-resolution links vinculin localization to function in focal adhesions. *Nat. Cell Biol.* **17**, 845–847 (2015).
66. Bays, J. L. & DeMali, K. A. Vinculin in cell–cell and cell–matrix adhesions. *Cell Mol. Life Sci.* **74**, 2999–3009. <https://doi.org/10.1007/s00018-017-2511-3> (2017).
67. Tochio, T., Tanaka, H., Nakata, S. & Hosoya, H. Fructose-1,6-bisphosphate aldolase A is involved in HaCaT cell migration by inducing lamellipodia formation. *J. Dermatol. Sci.* **58**, 123–129. <https://doi.org/10.1016/j.jdermsci.2010.02.012> (2010).
68. Kusakabe, T., Motoki, K. & Hori, K. Mode of interactions of human aldolase isozymes with cytoskeletons. *Arch. Biochem. Biophys.* **344**, 184–193. <https://doi.org/10.1006/abbi.1997.0204> (1997).
69. Harris, S. J. & Winzor, D. J. Enzyme kinetic evidence of active-site involvement in the interaction between aldolase and muscle myofibrils. *Biochim. Biophys. Acta* **91**, 121–126. [https://doi.org/10.1016/0167-4838\(87\)90279-2](https://doi.org/10.1016/0167-4838(87)90279-2) (1987).
70. Geng, S. et al. Deletion of TECRL promotes skeletal muscle repair by up-regulating EGR2. *Proc. Natl. Acad. Sci. U. S. A.* **121**, e2317495121. <https://doi.org/10.1073/pnas.2317495121> (2024).
71. Micera, A. et al. Toll-like receptors and tissue remodeling: The pro/cons recent findings. *J. Cell Physiol.* **231**, 531–544. <https://doi.org/10.1002/jcp.25124> (2016).
72. Hermida-Nogueira, L., Blanco, J. & García, Á. Secretome profile of leukocyte-platelet-rich fibrin (L-PRF) membranes. *Methods Mol. Biol.* **2628**, 207–219. [https://doi.org/10.1007/978-1-0716-2978-9\\_14](https://doi.org/10.1007/978-1-0716-2978-9_14) (2023).
73. Broeckx, S. et al. Allogenic mesenchymal stem cells as a treatment for equine degenerative joint disease: A pilot study. *Curr. Stem Cell Res. Ther.* **9**, 497–503. <https://doi.org/10.2174/1574888x09666140826110601> (2014).
74. Fujioka-Kobayashi, M. et al. Optimized platelet-rich fibrin with the low-speed concept: Growth factor release, biocompatibility, and cellular response. *J. Periodontol.* **88**, 112–121. <https://doi.org/10.1902/jop.2016.160443> (2017).
75. Covelli, V. et al. Salicylic acid release from syndiotactic polystyrene staple fibers. *Molecules* **28**, 5095. <https://doi.org/10.3390/molecules28135095> (2023).
76. Ogorevc, J., Lapanja, T., Poklukar, K., Tominšek, N. & Dovč, P. Establishment of primary keratinocyte culture from horse tissue biopsates. *Acta Agric. Slov.* **106**, 87–91. <https://doi.org/10.14720/aas.2015.106.2.3> (2015).
77. Madelaire, C. B., Klink, A. C., Israelsen, W. J. & Hindle, A. G. Fibroblasts as an experimental model system for the study of comparative physiology. *Comp. Biochem. Physiol. Part B: Biochem. Mol. Biol.* <https://doi.org/10.1016/j.cbpb.2022.110735> (2022).
78. Di Prima, G. et al. Green extraction of polyphenols from waste bentonite to produce functional antioxidant excipients for cosmetic and pharmaceutical purposes: A waste-to-market approach. *Antioxidants* **11**, 2493. <https://doi.org/10.3390/antiox11122493> (2022).
79. Jung, K. M. Betaine enhances the cellular survival via mitochondrial fusion and fission factors, MFN2 and DRP1. *Anim. Cells Syst. (Seoul)* **22**, 289–298. <https://doi.org/10.1080/19768354.2018> (2018).
80. Carbone, D. et al. Metabolomics-assisted discovery of a new anticancer GLS-1 inhibitor chemotype from a nortopsentin-inspired library: From phenotype screening to target identification. *Eur. J. Med. Chem.* **234**, 114233. <https://doi.org/10.1016/j.ejmech.2022.114233> (2022).
81. Franken, N. A., Rodermond, H. M., Stap, J., Haveman, J. & van Bree, C. Clonogenic assay of cells in vitro. *Nat. Protoc.* **1**, 2315–2319. <https://doi.org/10.1038/nprot.2006.339> (2006).
82. Rapa, S. F. et al. Plumericin protects against experimental inflammatory bowel disease by restoring intestinal barrier function and reducing apoptosis. *Biomedicines* **9**, 67. <https://doi.org/10.3390/biomedicines9010067> (2021).
83. Ostacolo, C. et al. Identification of an indol-based multi-target kinase inhibitor through phenotype screening and target fishing using inverse virtual screening approach. *Eur. J. Med. Chem.* **167**, 61–75. <https://doi.org/10.1016/j.ejmech.2019.01.066> (2019).
84. De Vita, S. et al. 2-Substituted 1,5-benzothiazepine-based HDAC inhibitors exert anticancer activities on human solid and acute myeloid leukemia cell lines. *Bioorg. Med. Chem.* **93**, 117444. <https://doi.org/10.1016/j.bmc.2023.117444> (2023).
85. Aquino, G. et al. Optimization of microwave-assisted extraction of antioxidant compounds from spring onion leaves using Box-Behnken design. *Sci. Rep.* **13**, 14923. <https://doi.org/10.1038/s41598-023-42303-x> (2023).
86. Izdebska, M. et al. Lidocaine induces protective autophagy in rat C6 glioma cell line. *Int. J. Oncol.* **54**, 1099–1111. <https://doi.org/10.3892/ijo.2018.4668> (2019).
87. Wang, Y. Y., Lee, K. T., Lim, M. C. & Choi, J. H. TRPV1 antagonist DWP05195 induces ER stress-dependent apoptosis through the ROS-p38-CHOP pathway in human ovarian cancer cells. *Cancers* **12**, 1702. <https://doi.org/10.3390/cancers12061702> (2020).
88. Amodio, G. et al. PERK-mediated unfolded protein response activation and oxidative stress in PARK20 fibroblasts. *Front. Neurosci.* **13**, 673. <https://doi.org/10.3389/fnins.2019.00673> (2019).
89. Colarusso, C. et al. Activation of the AIM2 receptor in circulating cells of post-COVID-19 patients with signs of lung fibrosis is associated with the release of IL-1 $\alpha$ , IFN- $\alpha$  and TGF- $\beta$ . *Front. Immunol.* **13**, 934264. <https://doi.org/10.3389/fimmu.2022.934264> (2022).
90. Trentini, M. et al. Link between organic nanovesicles from vegetable kingdom and human cell physiology: Intracellular calcium signalling. *J. Nanobiotechnol.* **22**, 68. <https://doi.org/10.1186/s12951-024-02340-8> (2024).
91. Viode, A. et al. A simple, time- and cost-effective, high-throughput depletion strategy for deep plasma proteomics. *Sci. Adv.* **9**, ead9717. <https://doi.org/10.1126/sciadv.adf9717> (2023).
92. Capaci, V. et al. The deep proteomics approach identified extracellular vesicular proteins correlated to extracellular matrix in type one and two endometrial cancer. *Int. J. Mol. Sci.* **25**, 4650. <https://doi.org/10.3390/ijms25094650> (2024).

## Author contributions

V.V. conceived the project, designed the experiments and drafted the manuscript. M.R.M., C.M., V.G. conducted the experiments and analysed data. C.D.P., T.C., G.P., M.D.C., D.D.B. collected and analysed samples. V.V., E.S., A.B., P.C., M.P.P. performed funding acquisition, project administration, data curation, writing-review & editing and conceptualization, and supervision of the study.

## Funding

This work was funded by Project IR0000028—“Pathogen readiness platform for CERIC–ERIC Upgrade” PRP@CERIC CUP: J97G22000400006. This study was also supported by the doctoral research funds of the Department of Veterinary Medicine and Animal production of the University of Naples Federico II, allocated to Chiara Montano.

## Declarations

### Competing interests

The authors declare no competing interests.

### Additional information

**Supplementary Information** The online version contains supplementary material available at <https://doi.org/10.1038/s41598-025-01820-7>.

**Correspondence** and requests for materials should be addressed to V.V.

**Reprints and permissions information** is available at [www.nature.com/reprints](http://www.nature.com/reprints).

**Publisher's note** Springer Nature remains neutral with regard to jurisdictional claims in published maps and institutional affiliations.

**Open Access** This article is licensed under a Creative Commons Attribution-NonCommercial-NoDerivatives 4.0 International License, which permits any non-commercial use, sharing, distribution and reproduction in any medium or format, as long as you give appropriate credit to the original author(s) and the source, provide a link to the Creative Commons licence, and indicate if you modified the licensed material. You do not have permission under this licence to share adapted material derived from this article or parts of it. The images or other third party material in this article are included in the article's Creative Commons licence, unless indicated otherwise in a credit line to the material. If material is not included in the article's Creative Commons licence and your intended use is not permitted by statutory regulation or exceeds the permitted use, you will need to obtain permission directly from the copyright holder. To view a copy of this licence, visit <http://creativecommons.org/licenses/by-nc-nd/4.0/>.

© The Author(s) 2025